CrystEngComm

This article can be cited before page numbers have been issued, to do this please use: M. Zeeshan, M. Y. Khan, M. Shahid, M. Khalid Parvez and X. Li, *CrystEngComm*, 2025, DOI: 10.1039/D5CE00684H.

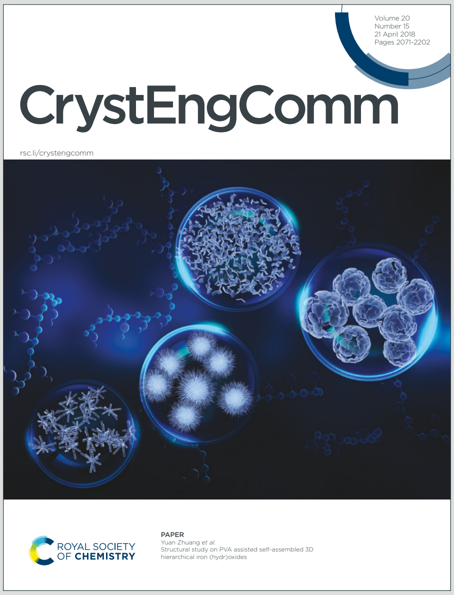

ROYAL SOCIETY OF CHEMISTRY

rsc.li/crystengcomm

View Article Online
DOI: 10.1039/D5CE00684H

Tailored nanoporous composite of bimetallic Zn-based MOF featuring two rare-metal geometries for organic dye sequestration: A mechanistic and kinetic insight into wastewater remediation

Mohd Zeeshan[a], Mohammad Yasir Khan[a], M. Shahid*[a], Mohammad Khalid Parvez[b], Xiang Li[c]

[a]*Functional Inorganic Materials Lab (FIML), Department of Chemistry, Aligarh Muslim University, Aligarh 202002, India.*
[b]*Department of Pharmacognosy, College of Pharmacy, King Saud University, Riyadh 11451, Saudi Arabia.*
[c]*Jiangsu Key Laboratory of Pesticide Science and Department of Chemistry, College of Science, Nanjing Agricultural University, Nanjing, 210095, China.*

**Corresponding Author; E-mail: shahid81chem@gmail.com (M. Shahid)*

Abstract

In the relentless pursuit of next-generation materials for sustainable water purification, we report the synthesis of a novel metal organic framework i.e., $\{(Me_2NH_2)_2[Zn_3(tpa)_4](DMF.3H_2O)\}_n$ **(ZS-4)** synthesized using terephthalic acid (H_2TPA). This framework elegantly integrates two crystallographically distinct zinc coordination environments (tetrahedral and octahedral), leading to an unusual and noteworthy outcome of (3,6)-connected *bcg* and *bct* topologies. To further enhance its functional attributes, a hybrid composite, **ZS-4@CNT**, was engineered by interacting carbon nanotubes (CNTs) into the pristine **ZS-4** matrix, resulting in notable improvements in physicochemical performance. Characterization was performed using FTIR, TGA, PXRD, SEM, TEM, BET, and XPS substantiated the structural integrity, thermal robustness, morphological uniformity, and surface chemistry of both materials. BET analysis revealed surface areas of 923.49 m^2/g for **ZS-4** and 1200.30 m^2/g for **ZS-4@CNT**. The BJH pore size distribution displayed narrow peaks at 5.2 nm and 5.5 nm, respectively, confirming enhanced mesoporosity in the composite. XPS data revealed peaks at 284.6 eV (C–C/C=C), 286.0 eV (C–O/C–OH), and 288.5 eV (O–C=O) in the C 1s spectrum. The O 1s region showed peaks at 531.8 eV (C=O) and 533.0 eV (C–OH). Zn 2p peaks at 1022.8 eV and 1042.7 eV confirmed the presence of Zn^{2+}. The **ZS-4@CNT** composite demonstrated a remarkable dye removal performance within the first 20 minutes, achieving 66% removal efficiency for methylene blue (MB). In comparison, under the same pH and temperature conditions, the removal efficiency for methyl orange (MO) was notably lower at 36.3%. The adsorption capacities were evaluated

View Article Online
DOI: 10.1039/D5CE00684H

using MB and MO as model pollutants, where **ZS-4** demonstrated uptakes of 72.35 mg/g for MB and 42.23 mg/g for MO, while **ZS-4@CNT** exhibited significant adsorption capacities of about 114.45 mg/g for MB and 43.15 mg/g for MO. Kinetic modeling adhered to a pseudo-second order framework, indicating chemisorption as the prevailing mechanism.

Keywords: *Metal-organic frameworks (MOFs), Methylene blue (MB), Methyl orange (MO), XPS, Green chemistry, Water remediation.*

1. Introduction

The exponential expansion of industrialization and urbanization over the past few decades has significantly strained natural ecosystems, with water pollution emerging as one of the most critical and persistent challenges. Among various forms of aquatic contaminants, synthetic dyes discharged from industrial effluents are particularly concerning due to their toxicity, chemical stability, and recalcitrant nature.[1-4] These dyes, primarily released by textile, paper, cosmetics, food processing, and pharmaceutical industries, impart intense coloration to water bodies, thereby reducing sunlight penetration, disrupting photosynthesis, and severely damaging aquatic life. Moreover, even at trace concentrations, many synthetic dyes have been found to be carcinogenic, mutagenic, or otherwise hazardous to human and environmental health. Their structural complexity, high solubility, and resistance to biodegradation pose serious limitations to conventional wastewater treatment systems, thus necessitating the development of efficient and sustainable removal strategies.[5-7] Among the numerous dyes released into wastewater, methylene blue (MB) and methyl orange (MO) have been widely used as model pollutants in environmental remediation studies. MB, a cationic thiazine dye, and MO, an anionic azo dye, differ significantly in terms of their molecular structure, charge distribution, and interaction mechanisms with adsorbent surfaces. Their chemical stability and structural diversity make them ideal representatives for testing adsorbent efficiency across a broad spectrum of dye types. However, their persistence in aquatic systems, coupled with potential toxic effects, highlights the urgent need for robust and broadly applicable removal technologies. Existing treatment methods such as photocatalysis, ozonation, advanced oxidation processes, membrane filtration, electrochemical degradation, and biological treatments often face challenges including high cost, limited degradation efficiency, generation of secondary pollutants, or narrow applicability to specific dye types.[8-11]

In this context, adsorption has emerged as one of the most promising approaches for dye removal due to its simplicity, low operational cost, environmental compatibility, and

DOI: 10.1039/D5CE00684H

efficiency across a wide range of contaminants. However, the success of adsorption-based methods critically depends on the selection of suitable adsorbent materials. The ideal adsorbent should possess high surface area, tunable pore structure, chemical functionality, and thermal and mechanical stability, while being cost-effective and environmentally benign. Conventional adsorbents such as activated carbon, zeolites, and clays, though widely studied, often suffer from limitations such as low adsorption capacities, poor regeneration, or lack of selectivity toward various dye molecules.[12-14]

In recent years, metal–organic frameworks (MOFs)[15-18] have emerged as a class of next-generation porous materials offering unprecedented opportunities for environmental remediation, especially in the area of dye adsorption[19-24]. They offer a versatile and tunable platform for the rational design of advanced adsorbents capable of selective dye capture. Beyond dye removal, their unique structural features have enabled a wide range of applications, including iodine sequestration[25-28], heavy metal capture, energy storage[29-31], fuel desulfurization[32], and carbon dioxide fixation[33], highlighting their broad potential in environmental and energy-related technologies. MOFs are crystalline structures composed of metal ions or clusters coordinated with multidentate organic ligands, forming highly ordered, tunable, and porous frameworks.[34] Their unique advantages include ultra-high surface areas, precisely controllable pore dimensions, tunable surface functionality, and diverse structural motifs. These features enable MOFs to interact with dye molecules via multiple mechanisms such as electrostatic attraction, hydrogen bonding, π–π stacking, and size-selective entrapment. Moreover, MOFs can be designed to simultaneously target both cationic and anionic dyes, making them ideal candidates for treating complex dye mixtures in industrial effluents.[35] Among the diverse range of MOFs, Zn-based MOFs have attracted considerable interest owing to their low toxicity, environmental friendliness, relative abundance, and ease of synthesis. Zinc is a biocompatible and sustainable metal that forms stable coordination networks, especially with carboxylate-based linkers. Zn(II) ions exhibit strong affinity for such ligands, facilitating the formation of robust, crystalline frameworks under mild, green synthesis conditions.[36-38] These properties make Zn-MOFs particularly well-suited for aqueous-phase applications, including dye adsorption. Additionally, the modular nature of MOF synthesis allows for post-synthetic modification or composite formation with other functional materials, offering further opportunities to enhance their adsorption performance, stability, and recyclability.[39-41] Terephthalic acid (H_2TPA) is one of the most extensively used dicarboxylate linkers in MOF chemistry due to its rigid, linear geometry and strong coordination ability with metal ions. The aromatic nature of H_2TPA facilitates π–π

View Article Online
DOI: 10.1039/D5CE00684H

interactions with aromatic dye molecules, while the carboxylate functionalities enable hydrogen bonding and electrostatic interactions. These features collectively enhance the dye adsorption capacity of MOFs built using this linker. Furthermore, frameworks constructed from Zn(II) and H_2TPA often exhibit high porosity, structural rigidity, and excellent chemical and thermal stability, making them promising candidates for practical water purification applications.[42-25]

Despite these advantages, several challenges remain in the practical deployment of MOFs for water treatment. Many reported systems involve complex or costly synthetic procedures, toxic organic solvents, or poor scalability, which limit their applicability in real-world scenarios. Moreover, while numerous MOFs show high efficiency for either cationic or anionic dye adsorption, relatively few materials have demonstrated the ability to adsorb both types effectively. Therefore, the development of a dual-function adsorbent capable of simultaneously removing structurally diverse dyes such as MB and MO remains an underexplored but highly valuable research direction. Additionally, enhancing the dispersibility, structural integrity, and electron transport properties of MOFs in aqueous systems can further boost their performance in environmental applications.[46,47]

To address these challenges, the present study reports the synthesis of a green, cost-effective, and scalable Zn-based MOF with the chemical formula $\{(Me_2NH_2)_2[Zn_3(tpa)_4](DMF.3H_2O)\}_n$ **(ZS-4)**, using terephthalic acid (H_2TPA) as the organic linker. Building upon this MOF, we further developed a composite material by integrating multi-walled carbon nanotubes (CNTs) to produce **ZS-4@CNT**. The rationale for incorporating CNTs lies in their excellent mechanical strength, high aspect ratio, superior surface area, and ability to introduce additional π-conjugated systems that can interact with dye molecules. The hybridization of MOFs with CNTs offers a synergistic advantage—combining the structural tunability and porosity of MOFs with the conductivity, stability, and adsorption potential of CNTs. The synthesized materials, **ZS-4** and **ZS-4@CNT**, were extensively characterized using powder X-ray diffraction (PXRD), Fourier-transform infrared spectroscopy (FTIR), scanning and transmission electron microscopy (SEM/TEM), thermogravimetric analysis (TGA), Brunauer–Emmett–Teller (BET) surface area analysis, and zeta potential measurements. These characterizations confirmed the successful formation of highly crystalline, porous frameworks and the effective incorporation of CNTs within the composite matrix. Adsorption studies were carried out using MB and MO as representative dyes to evaluate the adsorptive performance of both the pristine MOF and its composite. The

View Article Online
DOI: 10.1039/D5CE00684H

effects of key operational parameters such as solution pH, initial dye concentration, contact time, temperature, and adsorbent dosage were systematically investigated. The results demonstrated excellent adsorption efficiency for both MB and MO, with the CNT composite exhibiting enhanced uptake capacity and faster adsorption kinetics, particularly for MB, due to stronger π–π interactions and improved accessibility of active sites. Furthermore, adsorption isotherm and kinetic models were applied to understand the interaction mechanisms and rate-determining steps of dye uptake. Thermodynamic parameters confirmed the spontaneous and endothermic nature of the adsorption process. Reusability studies revealed the high structural stability and regeneration potential of both materials, with minimal loss in adsorption capacity after multiple cycles, underscoring their suitability for long-term practical application. Interestingly, despite their high surface areas (923.49 m^2/g for **ZS-4** and 1200.30 m^2/g for **ZS-4@CNT**), a comparatively lower adsorption efficiency was observed for MO than MB, which was attributed to electrostatic repulsion between the negatively charged MO molecules and the MOF surface, as well as steric hindrance due to the larger molecular size of MO. This study not only advances the field of MOF-based adsorbents but also provides critical insights into structure–function relationships governing dye adsorption, laying a strong foundation for future development of versatile, high-performance materials for environmental remediation.

2. Experimental Section

2.1 Materials

All chemicals were of analytical grade and used without further purification. Zinc nitrate hexahydrate [$Zn(NO_3)_2\cdot 6H_2O$], carbon nanotubes (CNTs), terephthalic acid (H_2TPA), dimethylformamide (DMF), methylene blue (MB), and methyl orange (MO) were purchased from commercial suppliers and used as received. Double distilled water was used for all experiments.

2.2 Physical methods

Elemental microanalysis (EA) was carried out at the Micro-Analytical Laboratory, CDRI, Lucknow, India. FTIR spectra were recorded on a PerkinElmer Spectrum GX spectrophotometer using KBr pellets, spanning the range of 400–4000 cm^{-1}. Powder X-ray diffraction (PXRD) analysis was performed on a Miniflexll X-ray diffractometer with Cu-Kα radiation. Raman measurements were conducted on a Renishaw inVia confocal micro-Raman spectrometer (Renishaw, Pliezhausen, Germany) equipped with dual laser excitation sources at 532 nm and 785 nm. Thermal Gravimetric Analysis (TGA) spectrum was scanned employing TGA-50H instrument, with a heating rate of 20°C min^{-1} from room temperature to

800°C with the samples placed in platinum pans and subjected to continuous airflow. To investigate dye adsorption, X-ray photoelectron spectroscopy (XPS) was employed using a PHI-5400 instrument from Physical Electronics with an Al-Kα source. Low-pressure adsorption isotherms for N_2 were measured using a Micromeritics 3Flex analyzer. A liquid N_2 bath was used for measurements at 77 K, while a water circulator was used for experiments at 273, 283, and 298 K. The specific surface area (SSA) was determined using the Brunauer-Emmett-Teller (BET) method, and the pore size distribution was obtained using the Barrett-Joyner-Halenda (BJH) method. Helium gas was used to determine the dead space in all sorption analyses.

2.3 Single crystal X-ray diffraction (SCXRD) studies

Single crystal X-ray diffraction (SCXRD) analysis of the **ZS-4** was conducted using a Bruker-SMART APEX-CCD diffractometer at 100 K with monochromated Mo-Kα radiation ($\lambda = 0.71073$ Å) from a graphite source.[48] Crystal data was analyzed following the guidelines in the International Tables for X-ray Crystallography, which provided key parameters such as absorption coefficients, anomalous dispersion corrections, and atomic scattering factors. Data integration and reduction were carried out using SAINT software.[49] The SADABS program was employed to correct for empirical absorption effects[50] in the collected reflections, while XPREP was used to determine the appropriate space group.[51] The structures were solved using Olex2 and full-matrix least squares on F^2 (SHELXL-2014)[52], employing direct methods. Refinements to non-hydrogen atoms were performed using anisotropic displacement parameters. For **ZS-4**, three water, two dimethyl ammonium cations, and one dimethylformamide molecules are squeezed in the lattice environment in order to get better clarity in the crystal structure. The CCDC reference number for **ZS-4** is 2442520. The detailed crystal data and its refinement parameters for **ZS-4** are presented in **Table S1 (Supporting Information).**

2.4 Synthesis

2.4.1 Synthesis of $\{(Me_2NH_2)_2[Zn_3(tpa)_4](DMF.3H_2O)\}_n$ (ZS-4)

ZS-4 was prepared using a solvothermal synthetic route. Equimolar quantities of $Zn(NO_3)_2{\cdot}6H_2O$ (1 mmol) and H_2TPA (1 mmol) were dissolved in a mixed solvent system comprising DMF and deionized water in a 3:2 volume ratio under continuous stirring until a clear solution was obtained. The resulting solution was transferred to a Teflon-lined stainless-steel autoclave and heated at 120 °C for 72 hours. The resulting solid was recovered by filtration, followed by thorough washing with fresh DMF and deionized water to eliminate any unreacted precursors or by-products. The purified material was then dried under vacuum

View Article Online
DOI: 10.1039/D5CE00684H

at 60 °C for 12 hours, affording highly crystalline **ZS-4** with an overall yield of 92%. Elemental analysis (%) for **ZS-4**; exp. C = 43.70; H = 4.35; N = 3.98; calc. C = 43.73; H = 4.20; N = 3.92 (**Scheme 1**).

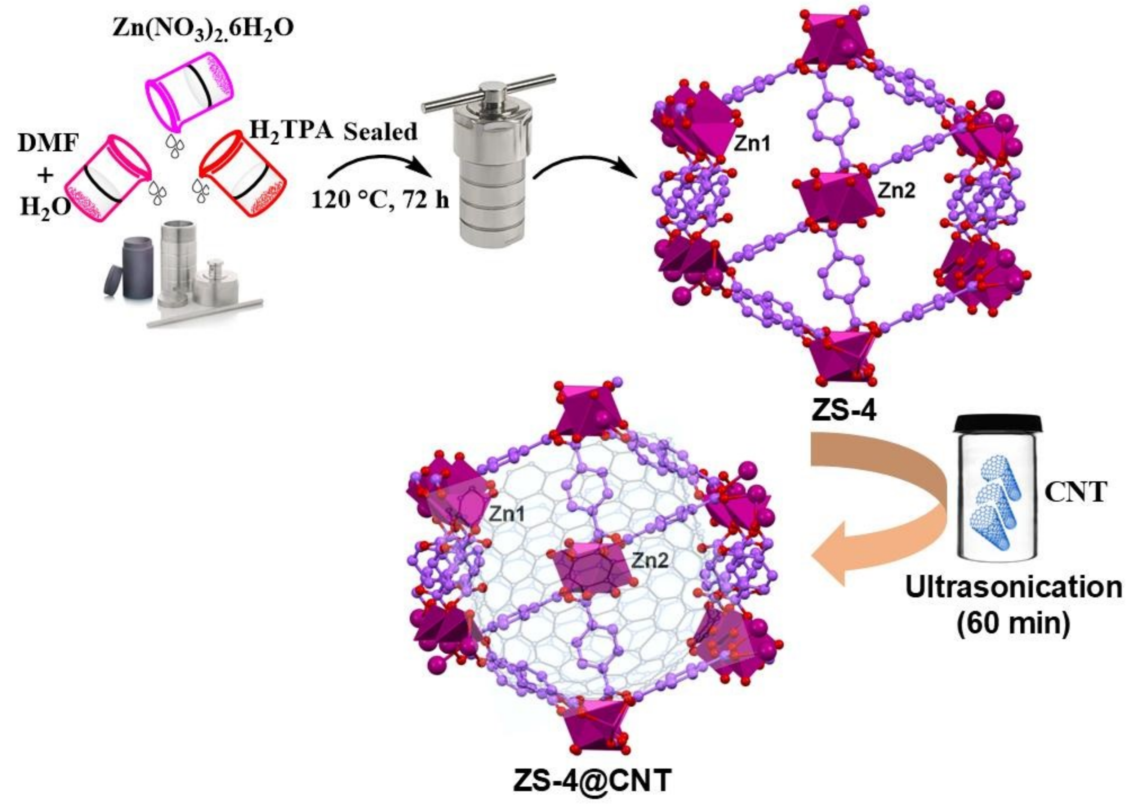

Scheme 1. Synthesis of **ZS-4** and **ZS-4@CNT.**

The coordination behavior of H_2TPA plays a pivotal role in dictating the structural topology and dimensionality of MOFs. Owing to its rigid linear geometry and bifunctional carboxylate groups located at para positions, H_2TPA acts as a versatile linker capable of adopting multiple coordination modes with metal centers. Upon deprotonation, the resulting tpa^{2-} ligand can coordinate to metal ions in a variety of binding fashions, such as monodentate, bidentate chelating, or bridging modes. In particular, the carboxylate groups can bridge adjacent metal centers, enabling the formation of extended one-dimensional chains, two-dimensional layers, or three-dimensional frameworks. The versatile coordination behavior of H_2TPA enables it to bridge various metal centers, making it a pivotal ligand in designing structurally and functionally diverse MOFs. The various coordination modes of H_2TPA with metal centres are depicted in the **Fig. S1 (Supporting Information).**

2.4.2 Modification of CNT into FCNTs

To introduce carboxyl (–COOH) functional groups onto the surface of pristine carbon nanotubes (CNTs), an acid treatment method was employed. Specifically, a known quantity of multi-walled carbon nanotubes (MWCNTs) was immersed in a 4 M nitric acid (HNO_3)

View Article Online
DOI: 10.1039/D5CE00684H

solution and subjected to ultrasonic agitation for 40 minutes using an ultrasonication bath. After sonication, the suspension was magnetically stirred at 50°C to promote efficient surface modification. This process led to the formation of a black, solid-like material. The resulting product was repeatedly washed with doubly distilled water to remove any residual acid, followed by drying in an oven at 80°C for 24 hours to yield the functionalized carbon nanotubes (FCNTs) ready for further use.

2.4.3 Synthesis of ZS-4@CNT nanocomposite

The **ZS-4@CNT** nanocomposite was synthesized *ex-situ* using the ultrasonication method. Initially, 0.005 g of CNTs were dispersed in a mixed solvent system comprising DMF:H_2O (3:2; v:v), followed by ultrasonication for 60 minutes to attain a uniform suspension. Further, a solution containing $Zn(NO_3)_2 \cdot 6H_2O$ (1 mmol) and H_2TPA (1 mmol), was prepared using a DMF:H_2O (3:2; v:v) and added to the above-prepared CNTs suspension, followed by an additional 10 minutes of ultrasonication to achieve thorough homogenization. The resulting mixture was heated at 120°C for 48 hours. Following the thermal treatment, the resulting black solid identified as the **ZS-4@CNT** nanocomposite was isolated by filtration, repeatedly washed with DMF and distilled water, and oven-dried at 100 °C for 12 hours. A schematic illustration of the synthesis pathway for the **ZS-4@CNT** nanocomposite is depicted in **Scheme 1**.

2.5 Dye adsorption experiments

To initiate the standard dye adsorption experiments, a 10 ppm stock solution of the dyes MB and MO was freshly prepared using double-distilled water. Subsequently, 10 mg of the **ZS-4** and **ZS-4@CNT** nanocomposite (in two different vials for checking adsorption capacities separately using UV-Vis technique) was introduced into 20 mL of this dye solution. Throughout the experiment, the both the suspensions were continuously stirred, and aliquots were periodically analysed at various intervals (0 to 180 minutes) using UV–Vis spectroscopy. Each sample was scanned individually across a wavelength range of 200–750 nm to monitor the adsorption progress. To adjust the pH of the dye solutions, small volumes of 0.1 M sodium hydroxide (NaOH) and 0.1 M hydrochloric acid (HCl) were employed, ensuring precise control over the reaction environment. The primary objective of these adsorption experiments was to evaluate the removal efficiency (R%) of the dyes by **ZS-4** and **ZS-4@CNT** nanocomposite individually. All assessments were performed following standardized protocols, and the experimental data were further interpreted using adsorption kinetic models.

The removal efficiency was calculated according to the following expression

View Article Online
DOI: 10.1039/D5CE00684H

$$\text{Removal efficiency } (\%\text{R}) = \frac{(C_o - C_e)}{C_o} \times 100 \qquad (1)$$

where C_o and C_e represent the initial and equilibrium concentrations of the dye (mg L^{-1}), respectively.[53] Furthermore, the influence of various parameters such as pH, temperature, and the presence of salts on the adsorption behavior and overall removal performance of the **ZS-4** and **ZS-4@CNT** composite were thoroughly investigated. These effects were systematically recorded by analysing the UV–Vis spectra of the filtrates collected after dye adsorption.

3. Results and Discussion

3.1 Crystal structure description of ZS-4

The single-crystal X-ray diffraction study of the **ZS-4** revealed that it crystallizes in the monoclinic crystal system with the *C2/c* space group. The asymmetric unit of the framework displayed three zinc atoms, fully deprotonated H_2TPA, coordinating oxygen atoms, and disordered solvent molecules within the pores. The empirical formula, $C_{39}H_{45}N_3O_{20}Zn_3$, corresponds to a molecular weight of 1070.32 g/mol. The unit cell parameters are a = 33.015(2) Å, b = 9.7380(6) Å, c = 18.1598(10) Å, with α = 90°, β = 95.296°, and γ = 90°, and a unit cell volume of 5813.5(6) $Å^3$, with Z = 4. Fractional Atomic Coordinates, equivalent isotropic displacement parameters, bond lengths, bond angles, etc. are shown in **Tables S2-S7 (Supporting Information)**. The zinc centers in the framework exhibit two distinct coordination geometries. Zn1 displays a distorted tetrahedral environment, being coordinated to four oxygen atoms from three independent H_2TPA linkers. The bond lengths between Zn1–O2, Zn1–O4 and Zn1–O6 are 1.95344, 1.97661 and 1.97276 Å, respectively; consistent with classical tetrahedral zinc carboxylate complexes. In contrast, Zn2 adopts a distorted octahedral geometry, bonded to six oxygen atoms from four different H_2TPA linkers.[54-56] The Zn2–O4, Zn2–O5 and Zn2–O8 bond distances are 2.20679, 2.03759 and 2.03772 Å, forming a stable coordination sphere that contributes to the rigidity of the 3D framework. Three dimensional frameworks of **ZS-4** along with other crystal structures including asymmetric unit are depicted in **Fig. 1.**

View Article Online
DOI: 10.1039/D5CE00684H

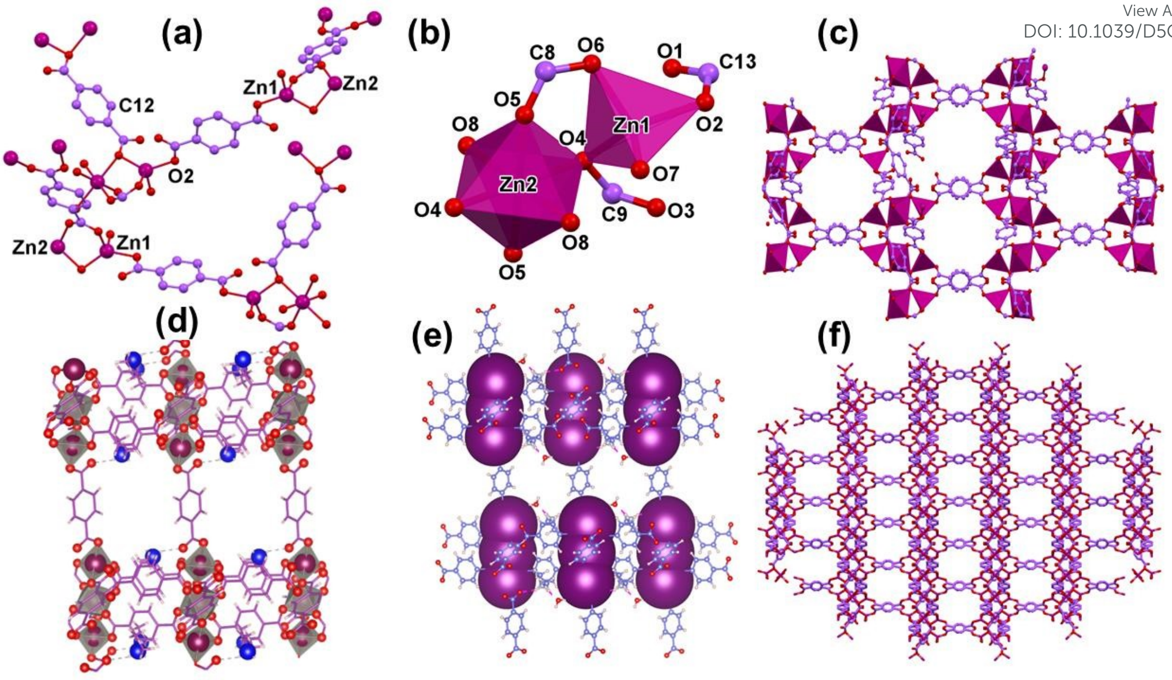

Fig. 1. Crystal structures showing **(a)** Coordination environment highlighting Zn1 (tetrahedral) and Zn2 (octahedral) centers bridged by H_2TPA; **(b)** Polyhedral representation **(c)** Three-dimensional framework; **(d)** Packing view; **(e)** Representation of the pore system and **(f)** Topological view of **ZS-4.**

Each H_2TPA bridges multiple Zn atoms through its bidentate carboxylate groups, generating an extended metal–ligand network. The μ_2-bridging coordination mode of the carboxylates facilitates strong Zn–O–C–O–Zn interactions and enables the propagation of connectivity throughout the structure. These linkages result in a three-dimensional porous architecture, where both tetrahedral and octahedral Zn nodes are interconnected by the rigid, planar aromatic linker. Within the channels of the framework, disordered solvent molecules such as dimethyl ammonium cations, H_2O and Me_2NCHO moieties are present.[57,58] These guests help maintain electroneutrality and may participate in hydrogen bonding with the carboxylate oxygen atoms of the framework, further stabilizing the crystal structure. Topological structures and pore architecture of the **ZS-4** showing (3,6)-connected *bcg* and *bct* nets, polyhedral structures, and space-filling models are displayed in **Fig. 2** and **Fig. S2-S6 (Supporting Information)**.

View Article Online
DOI: 10.1039/D5CE00684H

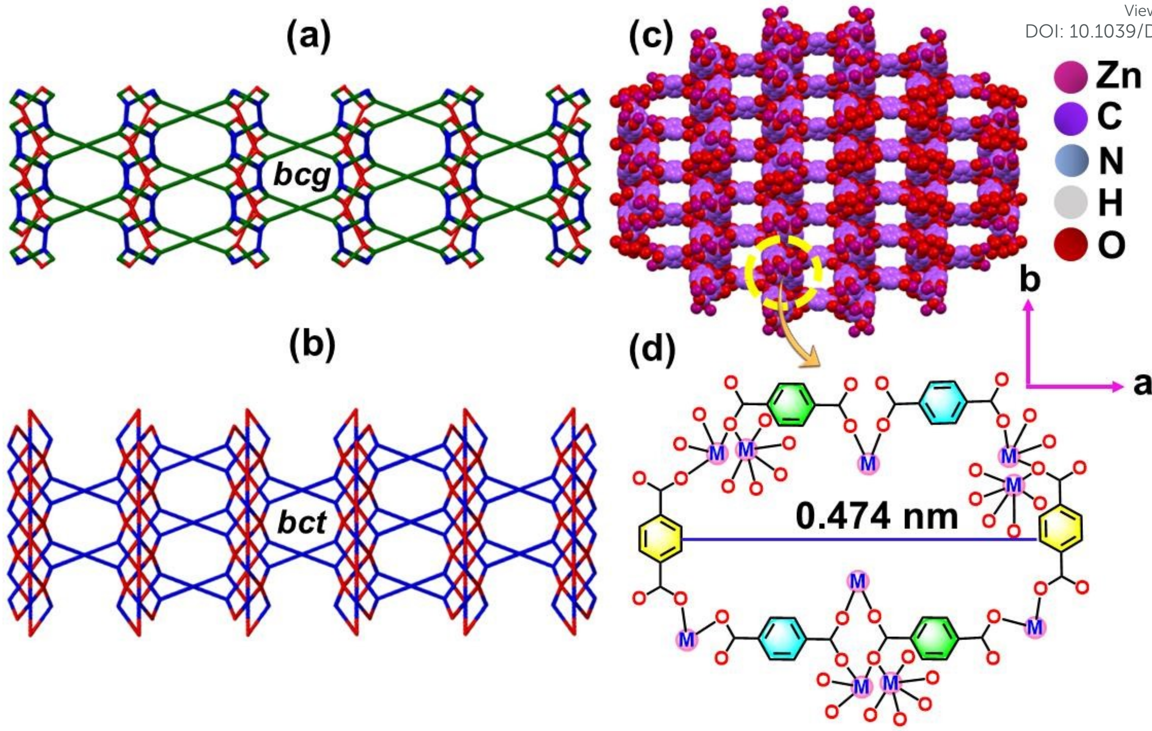

Fig. 2. Topological structures showing **(a)** *bcg* (body-centered cubic net with girder-like linkages) topology; **(b)** *bct* (body-centered tetragonal) topology; **(c)** Space-filling model and **(d)** Enlarged view of a single cyclic pore unit with a diameter of 0.474 nm along c axis**.**

The extended hydrogen-bonded coordination network in **ZS-4**, highlighting the spatial configuration and intermetallic distances within the framework, is illustrated in Fig. 3.

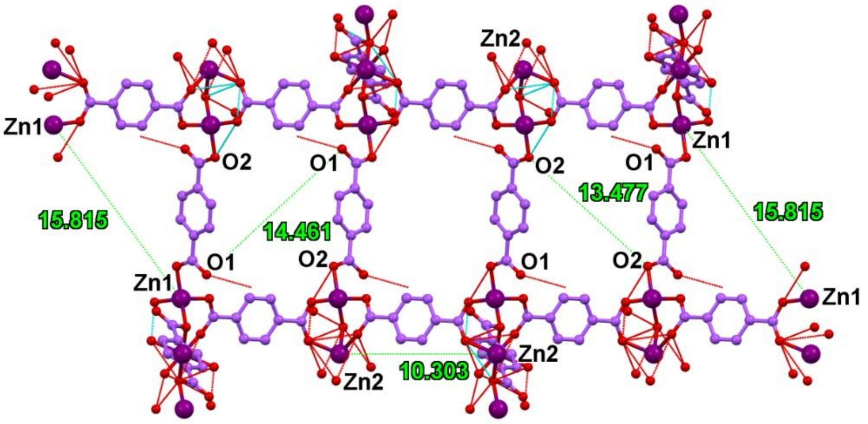

Fig. 3. Detailed view of the extended hydrogen bonded coordination network in **ZS-4**, emphasizing the spatial arrangement and intermetallic distances.

3.2 FTIR, PXRD, TGA and Raman studies

The FTIR spectra of **ZS-4**, CNT, and the **ZS-4@CNT** composite are shown in Fig. 4 (a). For the pristine **ZS-4**, the characteristic bands observed at 1580 cm^{-1} and 1370 cm^{-1} are attributed to the asymmetric ($\nu_{asy.}$) and symmetric (ν_{sym}) stretching vibrations of coordinated carboxylate ($-COO^{-}$) groups, respectively. The difference between these two bands, $\Delta\nu = 210$

DOI: 10.1039/D5CE00684H

cm^{-1}, suggests a monodentate coordination mode of carboxylate ligands to Zn^{2+} centers.[59,60] A sharp band at ~1665 cm^{-1} corresponds to coordinated DMF ($\nu_{C=O}$), while a broad band around 3420 cm^{-1} indicates the presence of hydroxyl groups or adsorbed water.[61] In the CNT spectrum, typical features such as the C=C stretching vibrations (~1580 cm^{-1}) and weak bands near ~3450 cm^{-1} (–OH) are observed. The composite **ZS-4@CNT** exhibits all the essential peaks of **ZS-4** and CNT, confirming the physical integration of the MOF and CNT components. Slight shifts in the carboxylate stretching bands in the composite indicate possible interfacial interactions between the MOF framework and CNTs.[62] These results confirm the successful coordination of terephthalic acid with Zn^{2+} ions and further support the structural integrity of the composite material (Fig. 4(a)).

Powder X-ray diffraction (PXRD) patterns of **ZS-4**, CNT, and the **ZS-4@CNT** composite are shown in Fig. 4, confirming the successful synthesis and crystallinity of the materials. **ZS-4** displays sharp and intense diffraction peaks at 2θ = 5.3°, 9.7°, 10.8°, 13.1°, and 17.5°, which can be indexed to the (200), (220), (222), (400), and (440) crystal planes, respectively (Fig. 4(b)). These well-resolved reflections are characteristic of a highly crystalline zinc-based MOF structure. The **ZS-4@CNT** composite retains all major reflections of pristine **ZS-4**, suggesting that the crystal structure remains intact upon CNT incorporation. Additional broad peaks at ~26° and ~43°, attributed to the (002) and (100) planes of CNTs, confirm their presence in the composite. No impurity peaks were observed, indicating phase purity. The patterns confirm that the structural integrity of **ZS-4** is preserved after compositing.[63-65]

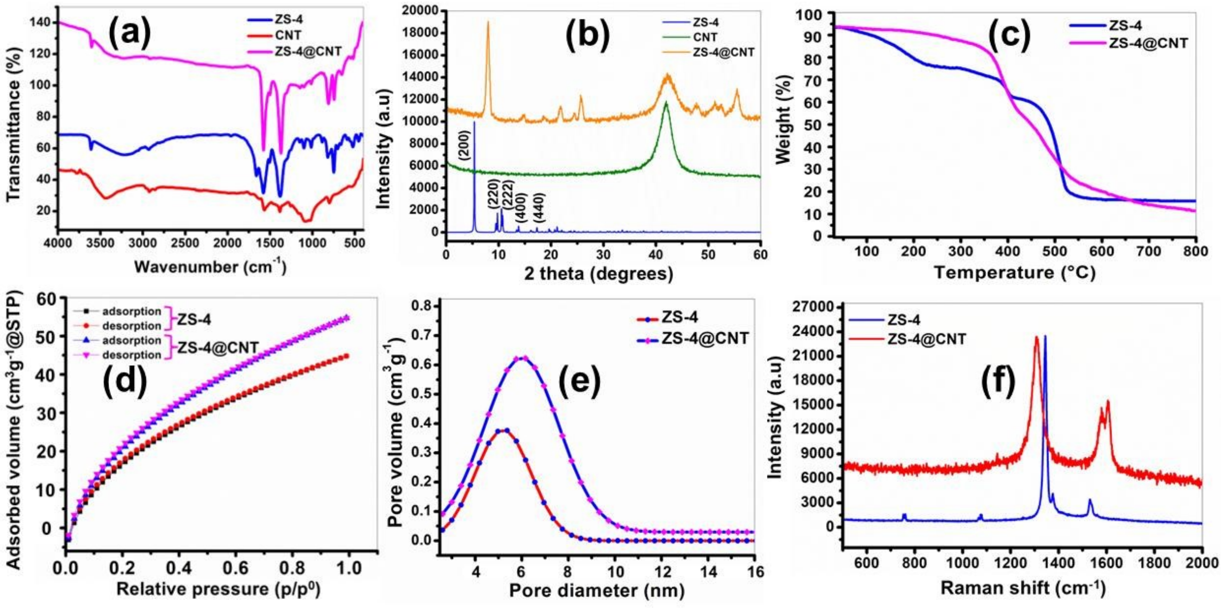

Fig. 4. **(a)** FTIR spectra; **(b)** PXRD plots; **(c)** TGA thermograms; **(d)** N_2 adsorption–desorption isotherms; **(e)** Pore size distribution curves and **(f)** Raman spectra of **ZS-4.**

TGA was performed to evaluate the thermal stability and decomposition behavior of the **ZS-4** and **ZS-4@CNT** in the temperature range of 80–800°C (**Fig. 4(c)**). For **ZS-4** (blue curve), an initial minor weight loss of up to 20.28% between 150–200°C is observed, corresponds to the decomposition of solvent molecules such as dimethyl ammonium cations, water and DMF. A gradual weight loss of up to 61.30% between 400–550°C is attributed to the partial decomposition of TPA that coordinated to the Zn^{2+} centers. Beyond 600°C, the weight stabilizes, suggesting the formation of thermally stable ZnO residue (18.22%). In the case of the **ZS-4@CNT** composite (magenta curve), a similar thermal profile is observed, but with distinct differences. The initial weight loss is slightly lower, implying improved moisture resistance due to the hydrophobic nature of CNTs. Notably, the major decomposition step is shifted toward a higher temperature range, and the rate of degradation is more gradual. This thermal delay highlights the enhanced thermal stability of the composite material, which can be attributed to the structural reinforcement and heat dissipation effect imparted by the carbon nanotubes.[66-68]

Raman spectroscopy was conducted to investigate the structural bands of **ZS-4** and **ZS-4@CNT**. **ZS-4** exhibits several sharp peaks, indicative of its well-defined crystalline nature. In contrast, the **ZS-4@CNT** composite shows two prominent peaks centered around 1350 cm^{-1} and 1580 cm^{-1}, corresponding to the D-band and G-band of carbon materials, respectively (**Fig. 4(f)**). The D-band arises from disordered or defect-containing carbon (sp^3 hybridized carbon), while the G-band is associated with the E_{2g} mode of graphitic carbon (sp^2 hybridization). The emergence of these bands in the **ZS-4@CNT** spectrum, which are absent in the pristine **ZS-4**, confirms the successful incorporation of CNTs into the MOF framework. Moreover, the enhanced intensity of these peaks suggests strong π–π interactions and possible charge transfer between the aromatic rings of the MOF's organic linker and the CNT surface. This structural integration is expected to improve the electrical conductivity, chemical stability, and overall performance of the material in dye adsorption.[69,70]

3.3 BET and XPS studies

Prior to nitrogen adsorption–desorption measurements, helium gas was employed to accurately determine the dead volume (non-adsorbing space) of the sample cell. This step is essential to ensure precise calculation of the adsorbed nitrogen volume, as helium, being non-adsorptive under experimental conditions, allows for the correction of void space within the system. The use of helium thus ensures the reliability and accuracy of the BET surface area and pore volume measurements. Further, BET isotherms were recorded for **ZS-4** and **ZS-4@CNT** at 77 K. The BET isotherm displayed type IV behavior for both **ZS-4** and **ZS-**

View Article Online
DOI: 10.1039/D5CE00684H

4@CNT, characteristic of mesoporous structures. The BET surface area of **ZS-4** was calculated to be 923.42 m^2/g, which significantly increased to 1200.30 m^2/g upon CNT incorporation. Corresponding BJH pore size distribution shows a narrow peak centered around 5.2 nm for **ZS-4** and 5.5 nm for **ZS-4@CNT**, confirming enhanced mesoporosity in the composite **(Fig. 4).** The increased surface area and pore volume in **ZS-4@CNT** suggest improved accessibility and diffusion pathways, beneficial for adsorption performance.[71-72]

X-ray photoelectron spectroscopy (XPS) was employed to elucidate the elemental composition and chemical states within the **ZS-4** framework. The survey spectrum **(Fig. 5(a))** confirms the presence of Zn, O, and C, consistent with the formation of a **ZS-4**. The deconvoluted C 1s spectrum **(Fig. 5(b))** reveals three primary peaks: 284.6 eV (C–C/C=C) from the aromatic linker backbone, 286.0 eV (C–O/C–OH) indicating the presence of hydroxyl or ether functionalities, and 288.5 eV (O–C=O) associated with carboxylate groups coordinated to the Zn centers. This clearly supports the successful incorporation of the H_2TPA into the MOF structure. Additionally, the O 1s spectrum **(Fig. 5(c))** displays two peaks at 531.8 eV and 533.0 eV, attributed to carbonyl oxygen (C=O) and hydroxyl/adsorbed oxygen species (C–OH or H_2O), respectively. High-resolution Zn 2p spectra **(Fig. 6(d))** exhibit two well-defined peaks at 1022.8 eV and 1042.7 eV, corresponding to Zn $2p_{3/2}$ and Zn $2p_{1/2}$, respectively, confirming the +2 oxidation state of zinc ions. These findings align well with the carboxylate coordination environment and further validate the structural integrity of the MOF.[73]

View Article Online
DOI: 10.1039/D5CE00684H

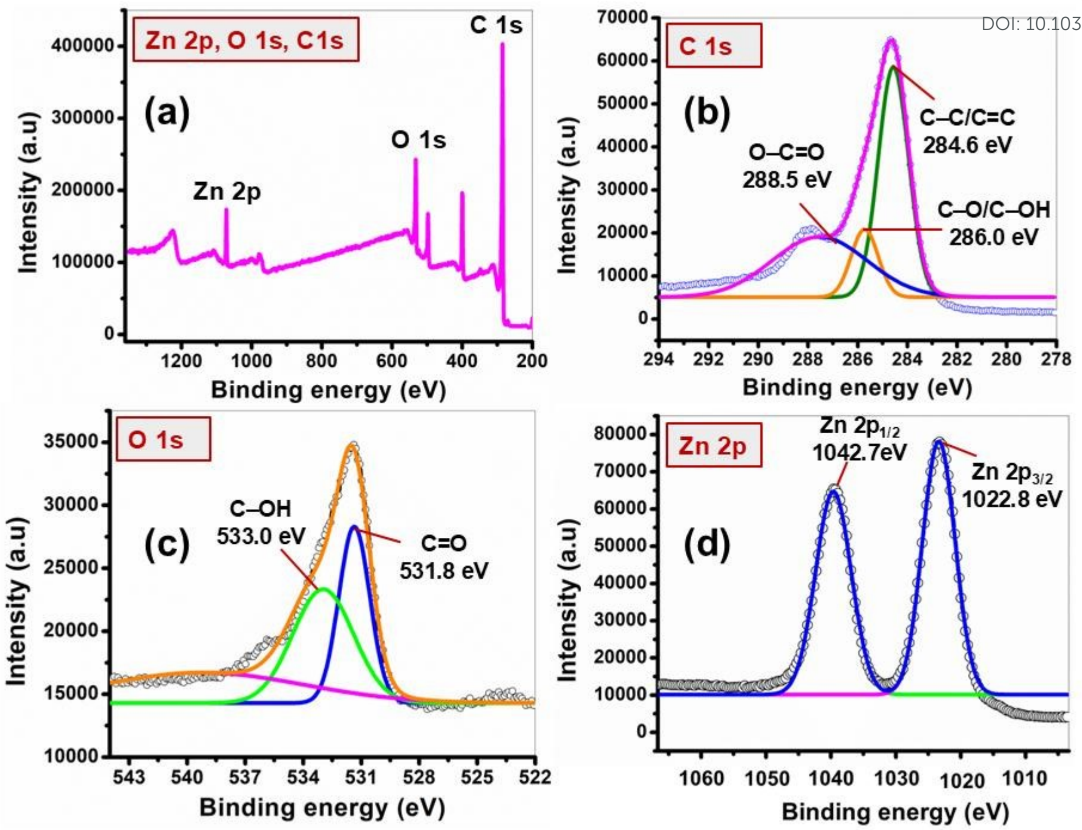

Fig. 5. XPS analysis showing **(a)** Wide-scan spectrum; **(b)** C 1s; **(c)** O 1s; and **(d)** Zn 2p of **ZS-4.**

3.4 SEM and TEM studies

The surface morphology and structural features of the synthesized materials were investigated through SEM, TEM, and SAED analyses. As shown in **Fig. 6(a–c)**, **ZS-4** exhibits well-developed polyhedral crystals with sharp edges and smooth surfaces, indicating uniform and controlled particle growth. At higher magnifications, a porous three-dimensional network becomes apparent, with polyhedral units interconnected to form a robust framework. The inset reveals sub-micron-sized pores (~1 μm), suggesting the material's high potential for adsorption applications. This interconnected architecture likely arises from the dual coordination behavior of Zn^{2+} ions; some adopting tetrahedral and others octahedral geometries leading to enhanced structural flexibility and mechanical integrity.[74]

View Article Online
DOI: 10.1039/D5CE00684H

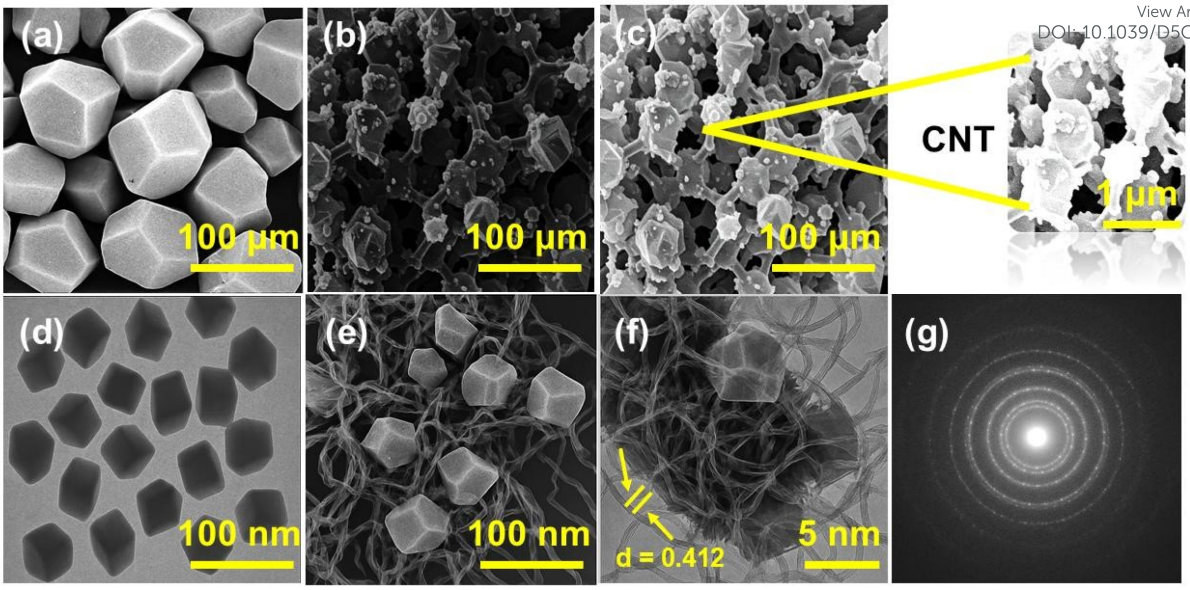

Fig. 6. Morphological analysis showing SEM of pristine **(a) ZS-4** crystals; **(b, c) ZS-4@CNT**; **(d)** TEM image of **ZS-4** crystals; **(e, f) ZS-4@CNT**, inset in; (f) Lattice fringes with interplanar spacing of 0.412 nm; and **(g)** SAED pattern of **ZS-4@CNT** with well-resolved diffraction rings.

Fig. 6(d–g) illustrates the internal morphology and structural features of the synthesized composite. The TEM images reveal well-defined polyhedral particles uniformly dispersed within a fibrous matrix, indicative of successful integration with carbon nanotubes. High-resolution imaging confirms the crystalline nature through visible lattice fringes with an interplanar spacing of 0.412 nm. Additionally, the SAED pattern displays sharp and concentric diffraction rings, reflecting the polycrystalline character and high structural order of the material.[75]

3.5 Adsorption of organic dyes

In the experimental procedure, 10 mg of the well-defined crystals of **ZS-4** and **ZS-4@CNT** were dispersed into a two different round-bottom flask containing 50 mL of dye solutions, including MB, and MO. The adsorption experiment was conducted for 180 minutes, during which a substantial portion of the dye molecules was adsorbed onto the polymer surfaces, as evidenced in **Fig. 7**. Stirring was maintained throughout the experiment, and 3 mL aliquots were periodically collected, centrifuged, and analysed using UV-visible spectrophotometry to monitor changes in dye concentration over time. The absorbance–wavelength spectra confirmed efficient dye adsorption, with both **ZS-4** and **ZS-4@CNT** showing notably high affinity for the cationic dye MB. While both materials could adsorb anionic dyes, they exhibited a stronger affinity for cationic dyes, primarily due to their structural architecture and surface functional groups.

View Article Online
DOI: 10.1039/D5CE00684H

The adsorption capacity can be calculated as:

$$\text{Adsorption capacity } (q_t) = \frac{(C_o - C_t)}{\text{m}} \times \text{V} \qquad (2)$$

The initial and final concentrations of the organic dyes, denoted as C_o and C_t (mg L^{-1}), m and V are the mass of adsorbent and volume of dye solutions, respectively, were used to assess the adsorption performance.[76] Analysis from **Fig. 7 (c, d)** reveals that MB exhibited significantly enhanced adsorption onto the composite frameworks comparatively than **ZS-4** (**Fig. 7 (a, b)**), attributed to their structural compatibility with the adsorbents. Over time, a progressive decline in the characteristic absorption peaks of MB (664 nm) and MO (460 nm) was observed, indicating efficient dye removal from the solution.

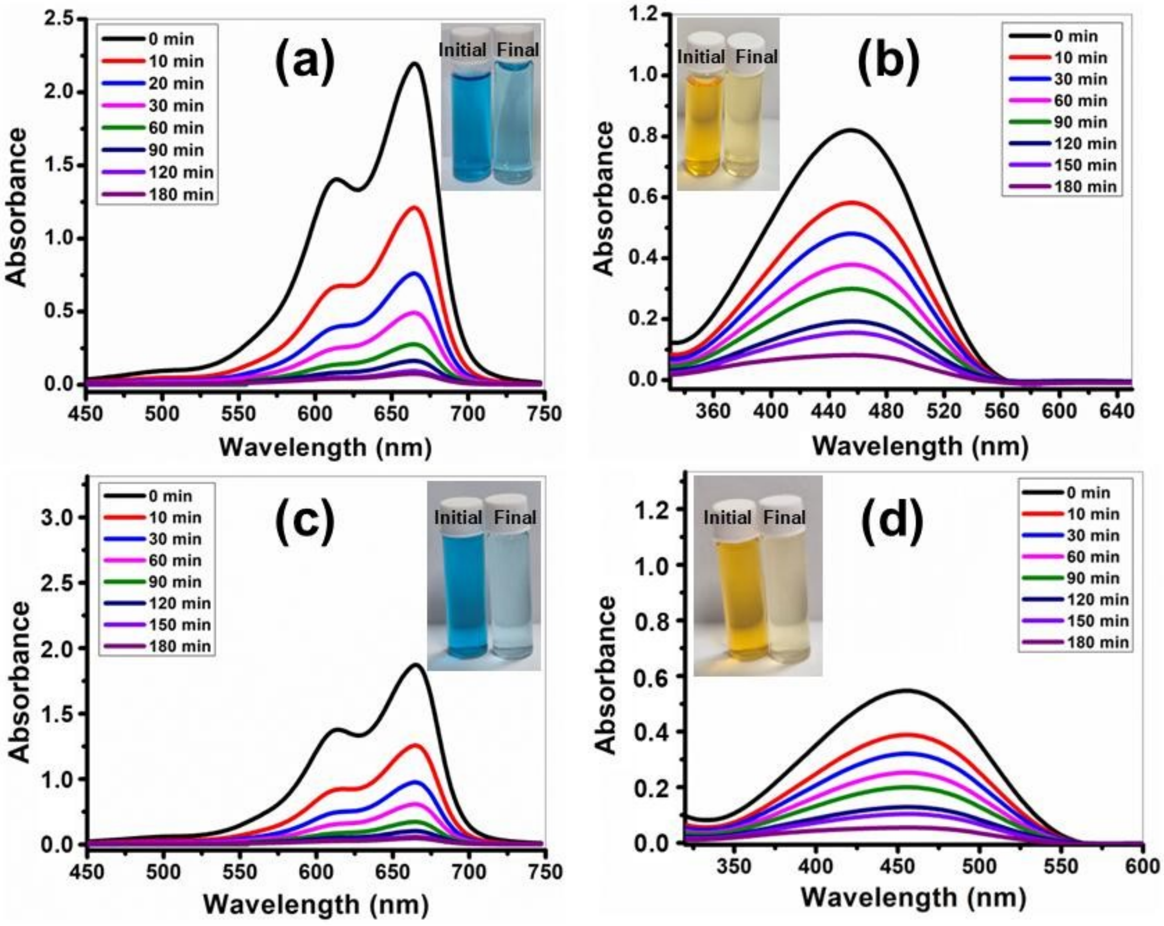

Fig. 7. Changes in UV-Vis spectra showing the adsorption of organic dye pollutants over time using MB and MO for **(a, b) ZS-4** and **(c, d) ZS-4@CNT**, inset in.

The superior adsorption capacities of **ZS-4@CNT** towards cationic dye, MB governed by strong hydrogen bonding, electrostatic attractions and π–π stacking interactions between the dye molecules and the composite networks comparatively than MO. The adsorption

View Article Online
DOI: 10.1039/D5CE00684H

performance of **ZS-4@CNT** toward dye removal was strikingly evident within the first 20 minutes, achieving a removal efficiency of 66% for MB **(Table 1).**

Table 1. Time-dependent removal efficiency (%R) of MB and MO dyes using **ZS-4** and **ZS-4@CNT** adsorbents over a period of 180 minutes.

ZS-4				**ZS-4@CNT**			
MB		**MO**		**MB**		**MO**	
Time (min)	%R	Time (min)	%R	Time (min)	%R	Time (min)	%R
0	0.00	0	0.00	0	0.00	0	0.00
10	43.6	10	15.1	10	45.5	10	17.3
20	58.2	20	32.5	20	66.0	20	36.3
30	72.5	30	47.7	30	77.3	30	50.0
60	82.8	60	62.6	60	88.7	60	67.3
90	88.5	90	72.7	90	92.3	90	77.6
120	90.5	120	80.2	120	95.5	120	82.8
180	90.9	180	81.2	180	96.9	180	86.3

In contrast, under identical pH and temperature conditions, the removal efficiency for MO was relatively lower, reaching 33.3%. MO is an anionic dye with a relatively large molecular structure, and its adsorption is strongly influenced by electrostatic interactions and steric accessibility. The framework of **ZS-4**, although porous, may possess a pore-limiting diameter that restricts the diffusion of larger dye molecules like MO into the internal pores leading to electrostatic repulsion with the anionic sulfonate groups of MO, thereby reducing the adsorption affinity. Furthermore, the larger hydrodynamic radius and slower diffusion rate of MO in aqueous solution contribute to kinetic limitations during the adsorption process. **ZS-4@CNT** exhibited an increased affinity toward MB dye, rapidly sequestering a significant amount within a short span of time. Over the course of 180 minutes, the system gradually reached adsorption equilibrium, with **ZS-4@CNT** attaining adsorption capacities of 114.45 mg/g for MB and 43.15 mg/g for MO (based on the calculations from equations 1 and 2). Meanwhile, the **ZS-4** counterpart exhibited lower equilibrium capacities of 72.35 mg/g and 42.23 mg/g for MB and MO, respectively, emphasizing the enhanced efficiency imparted by the CNT composite. This time-dependent decline in dye concentration, confirmed through UV–Vis spectral analysis, revealed a pronounced fading of MB's characteristic blue color to nearly colorless, while MO exhibited only a slight visual change (as shown in the insets of **Fig. 7 (a-d).** The superior performance of **ZS-4@CNT** in MB removal can be attributed to the strong electrostatic attraction between the positively charged MB molecules and the negatively charged surface functional groups of the nanocomposite in a neutral medium. In

View Article Online
DOI: 10.1039/D5CE00684H

contrast, MO, bearing a negative charge, undergoes electrostatic repulsion with the negatively charged adsorbent, thereby limiting its uptake. This fundamental difference in charge interactions explains the selective and more efficient adsorption behavior observed for MB over MO.

3.5.1 Separation of organic dyes

In continuation of the earlier observations, the synthesized **ZS-4** and **ZS-4@CNT** were further investigated as promising candidates for the adsorption and selective separation of aromatic dyes possessing different ionic charges, specifically MB as a cationic dye and MO as an anionic dye. To assess their separation capability, 20 mg of finely powdered **ZS-4** and **ZS-4@CNT** crystals were uniformly dispersed in aqueous solutions containing a mixture of MB and MO at room temperature. The adsorption behavior and selectivity were monitored in real time using UV-visible spectroscopic analysis. As illustrated in **Fig. 8**, a notable decrease in the characteristic absorption peaks corresponding to MB was observed progressively with the passage of time, indicating effective uptake of MB molecules by **ZS-4@CNT**. In contrast, the absorption bands associated with MO remained almost unchanged throughout the experiment, suggesting negligible interaction of MO with the polymeric frameworks under similar conditions. This differential behavior strongly implies a selective preference of the **ZS-4@CNT** towards cationic dyes over anionic counterparts. Further detailed analysis revealed that the adsorption of MB onto the **ZS-4@CNT** occurred exceptionally fast, with almost complete removal achieved within the first 5 minutes of contact. Meanwhile, the MO molecules largely remained in the solution phase during this period, confirming the ability of the **ZS-4@CNT** to discriminate between dyes based on their charge characteristics. This remarkable selectivity can be attributed to the favorable non-covalent interactions, such as electrostatic forces, hydrogen bonding, and π–π stacking, that exist between the electron-rich frameworks of the **ZS-4@CNT** and the electron-deficient MB molecules. Overall, these results demonstrate the potential application of these **ZS-4@CNT** not only for efficient dye removal but also for the selective separation of mixed dye systems, which is of significant importance for practical wastewater treatment and environmental remediation efforts.[77]

View Article Online
DOI: 10.1039/D5CE00684H

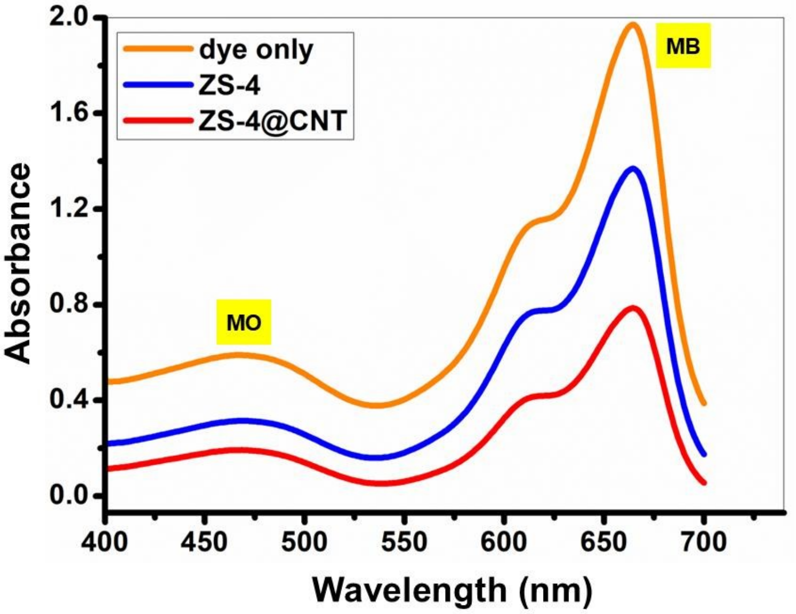

Fig. 8. Separation of organic dyes by **ZS-4** and **ZS-4@CNT.**

3.5.2 Effect of pH on the adsorption process

The adsorption process of dyes is profoundly influenced by several factors, including the surface charge of the adsorbent, the degree of dye ionization, and the nature of adsorbates present in wastewater, all of which are largely dependent on the solution pH. To investigate the pH effect, adsorption experiments were conducted over a pH range of 2–12, as illustrated in **Fig. 9 (a)**. The pH adjustments were carried out using 0.1 N HCl and 0.1 N NaOH under ambient conditions. From **Fig. 9 (a),** it is evident that the adsorption efficiency of methylene blue (MB) increased significantly as the pH rose from 2 to 7, achieving a maximum efficiency of approximately 98% at pH 7. Conversely, the adsorption of methyl orange (MO) peaked at around 72.12% at pH 5. Literature suggests that electrostatic interactions between the adsorbent and dye molecules play a critical role in dictating adsorption performance. In line with this, zeta potential measurements were employed to determine the surface charge characteristics of the synthesized materials. As presented in **Table 2**, the zeta potential of **ZS-4@CNT** was found to be negative at pH 7 and became progressively more negative at higher pH values. The zero point charge (pH_{zpc}) for the nanocomposite was determined to be pH 6. At pH values below pH_{zpc}, the surface carries a positive charge, which disfavours the adsorption of the cationic MB dye due to electrostatic repulsion. Notably, at pH values around the pK_a of MB (3.8), the dye exists in both undissociated (MB°) and cationic (MB^{+}) forms in equal proportions. At pH 3 and pH values above 6, the MB^{+} form becomes dominant.[78] Thus, at higher pH levels, the negatively charged adsorbent surface strongly

View Article Online
DOI: 10.1039/D5CE00684H

attracts the positively charged MB^+ species, leading to enhanced removal efficiencies. In contrast, for MO adsorption, lower pH conditions were favourable, with maximum adsorption observed at pH 5.

Table 2. Calculation of zeta potential of **ZS-4@CNT** at different pH.

pH	**Zeta potential (mV)**
2	0.23
3	0.22
4	0.21
5	0.20
6	0.0
7	-0.23
8	-0.32
9	-0.32
10	-0.33
11	-0.33
12	-0.32

Given that MO has a pK_a of 3.47, it predominantly exists in its neutral form (MO^o) below this pH, while at pH values above 3.47, it transitions to an anionic form (MO^-). Thus, within the pH range of 3.47–5, the positive surface charge of the nanocomposite favours the adsorption of the anionic MO dye through electrostatic attraction. However, as the pH increases beyond the pH_{zpc} (>6), the surface becomes increasingly negative, leading to electrostatic repulsion with the anionic MO^- species, thereby decreasing the adsorption efficiency. It is also important to highlight that the MB adsorption efficiency did not decline significantly even at pH values greater than 7, suggesting that mechanisms beyond electrostatic attraction, such as π–π stacking interactions between the aromatic rings of MB and the H_2TPA ligands in **ZS-4@CNT**, along with potential hydrogen bonding interactions, contribute significantly to the adsorption process.[79]

View Article Online
DOI: 10.1039/D5CE00684H

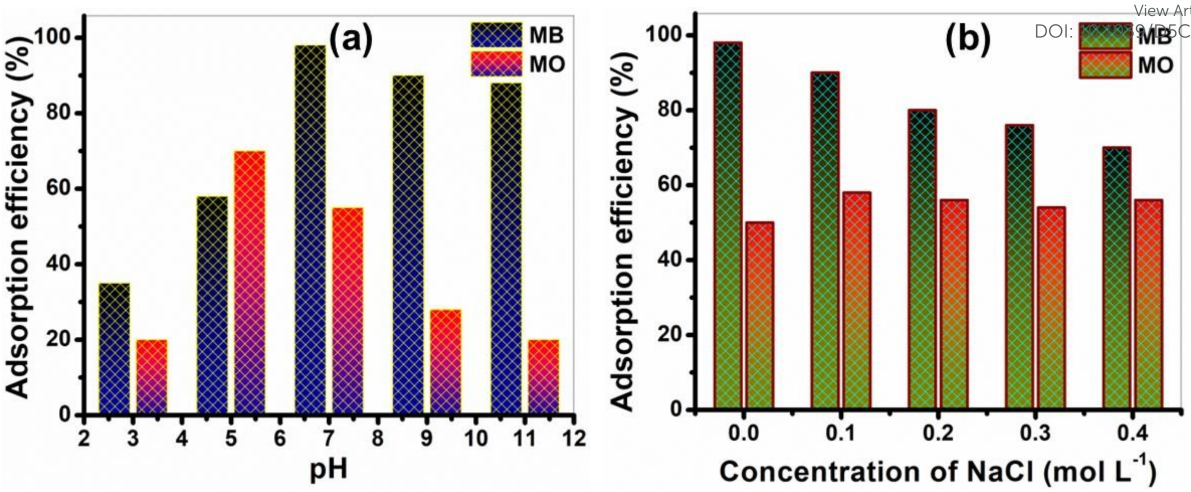

Fig. 9. Effect of (a) pH; and (b) NaCl concentration on the adsorption efficiency of MB and MO dyes using the synthesized **ZS-4@CNT.**

Considering that real industrial wastewater often contains high salt concentrations, the influence of ionic strength on dye adsorption was further examined. A series of adsorption experiments were performed at pH 7 with varying NaCl concentrations ranging from 0.0 to 0.4 mol/L, and the results are presented in **Fig. 9 (b).** In general, when electrostatic attractions dominate, an increase in ionic strength tends to reduce adsorption efficiency, whereas in cases of electrostatic repulsion, adsorption may improve with higher ionic strength. The experimental results showed a decline in MB adsorption efficiency with increasing salt concentration, attributed to the competitive interaction between Na^+ ions and MB molecules for the active adsorption sites. In contrast, MO adsorption efficiency slightly improved with increasing ionic strength. This can be rationalized by considering that Na^+ ions act as spacers, mitigating the electrostatic repulsion between the negatively charged adsorbent surface and the sulfonate groups of MO, thus facilitating enhanced adsorption through charge shielding effects.[80]

3.5.3 Effect of temperature

Temperature plays a pivotal role in determining the adsorption performance of porous materials, as it influences the interaction strength between adsorbent surfaces and dye molecules. In the present study, the temperature-dependent adsorption behavior of both **ZS-4** and **ZS-4@CNT** was evaluated for MB and MO dyes over a temperature range of 25–60 °C, as depicted in **Fig. 10 (a, b)**. The results clearly show that maximum adsorption efficiencies were achieved at room temperature (25 °C), with **ZS-4** reaching up to 90.5% for MB and 64.2% for MO, while **ZS-4@CNT** exhibited even higher efficiencies of 98.2% for MB and 70.4% for MO. A consistent decline in adsorption efficiency with rising temperature was

View Article Online
DOI: 10.1039/D5CE00684H

observed for both materials, indicative of an exothermic adsorption process where elevated thermal energy disrupts dye-adsorbent interactions, possibly through desorption or weakened electrostatic forces. Notably, the enhanced performance of **ZS-4@CNT** across all temperatures underlines the role of CNT incorporation in improving surface area and active site accessibility.[81]

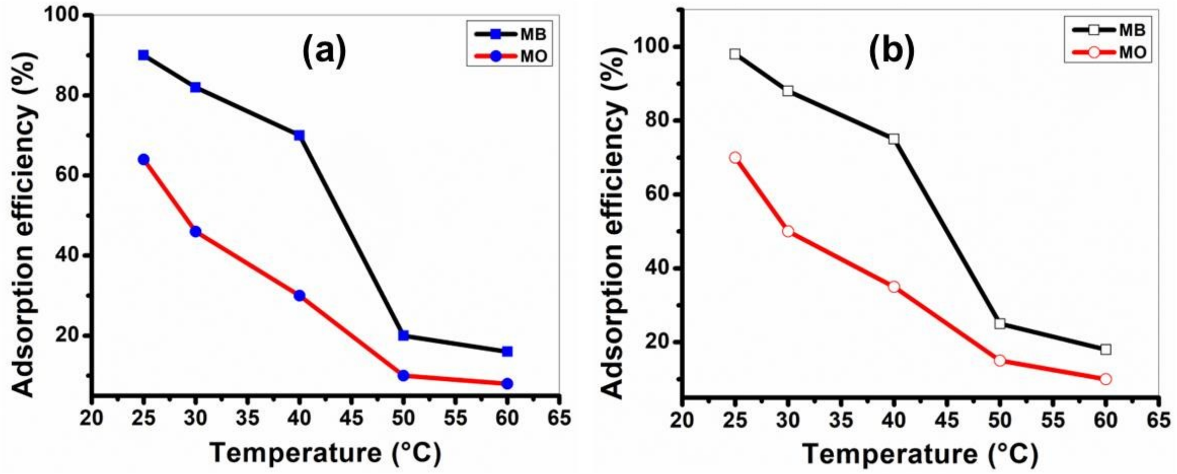

Fig. 10. Effect of temperature on the adsorption efficiency of MB and MO dyes for (a) **ZS-4**; and (b) **ZS-4@CNT**.

3.5.4 Recyclability of ZS-4 and ZS-4@CNT as adsorbents

To assess the reusability and stability of the **ZS-4** and **ZS-4@CNT** nanocomposite for the adsorption of MB and MO dyes, a series of cyclic adsorption–desorption experiments were performed. After each adsorption cycle, the used **ZS-4** and **ZS-4@CNT** material was carefully separated from the aqueous dye solution, thoroughly washed multiple times with dimethylformamide (DMF) and double-distilled water to remove any residual dye molecules, and subsequently dried in an oven at 90°C to restore its activity. The regenerated adsorbent was then subjected to fresh batch adsorption experiments under optimized conditions: an initial dye concentration of 10 ppm, a temperature of 25°C, and a pH of 7 for MB and 5 for MO, respectively. This process was repeated up to four consecutive cycles to evaluate the long-term performance and structural integrity of the adsorbent. The results, presented in **Fig. 11 (a, b)** and **Fig. S6. SI** clearly demonstrate that **ZS-4** and **ZS-4@CNT** maintained a remarkably high removal efficiency for MB even after four regeneration cycles, with only a marginal decline in adsorption capacity. This outstanding reusability highlights the robustness and resilience of the **ZS-4@CNT** framework, positioning it as a highly promising candidate for practical applications in wastewater treatment, particularly for cationic dye removal. Notably, the reusability performance surpasses many adsorbent materials previously reported in the literature, further validating its potential for real-world applications.[82-84]

View Article Online
DOI: 10.1039/D5CE00684H

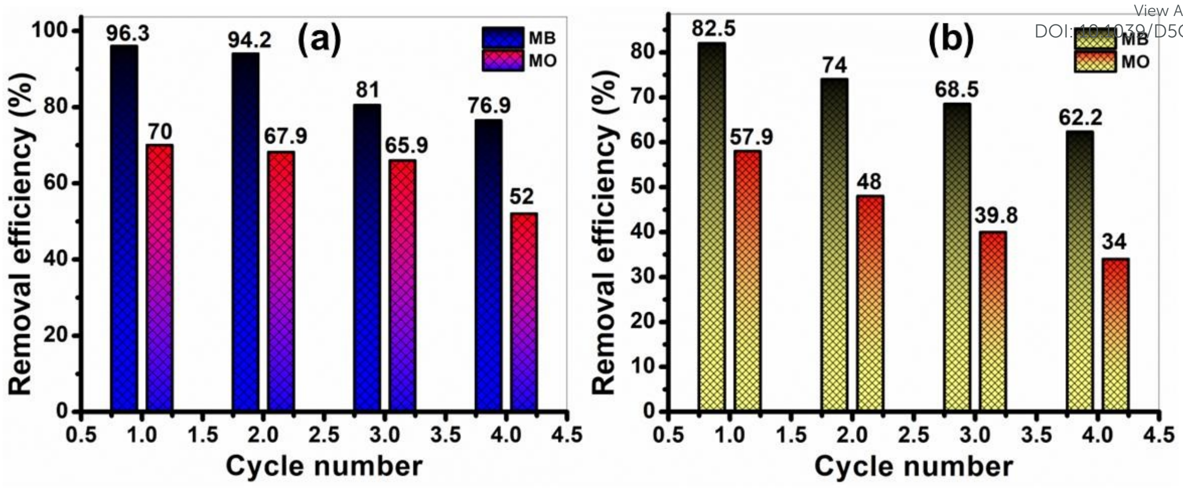

Fig. 11. Reusability performance for dye removal over four consecutive adsorption–desorption cycles for (a) **ZS-4@CNT**; and (b) **ZS-4**.

In contrast, the reusability performance toward MO dye was comparatively less satisfactory. The removal efficiency of MO declined noticeably after each regeneration cycle, indicating that the structural and surface properties of **ZS-4@CNT** may not be ideally suited for the repeated adsorption of anionic dyes. This reduced efficiency could be attributed to stronger dye-framework interactions or irreversible adsorption of MO molecules that hinder the regeneration of active sites. Consequently, while **ZS-4@CNT** demonstrates excellent durability for MB removal, its applicability for the repetitive removal of MO remains limited. Overall, the **ZS-4** and **ZS-4@CNT** nanocomposite exhibits exceptional regeneration ability and mechanical stability in the case of MB dye, making it a viable and sustainable adsorbent for practical water purification systems targeting cationic contaminants.

3.5.5 Adsorption kinetics

Given the significant adsorption of cationic dyes on the surfaces of **ZS-4** and **ZS-4@CNT**, it became imperative to delve deeper into the kinetics of the adsorption processes. To achieve a comprehensive understanding, the adsorption behavior over time was meticulously monitored, and kinetic analyses were performed using three distinct models: the pseudo-first-order model, the pseudo-second-order model, and the intraparticle diffusion model. The kinetic parameters for each model were calculated and are summarized in **Table 3.** The pseudo-first-order equation expressed as follows:

$$\log(q_e - q_t) = log\ q_e - \frac{k_1}{2.303}t \qquad (3)$$

View Article Online
DOI: 10.1039/D5CE00684H

where k_1 (min^{-1}) represents the rate constant, q_t is the adsorption capacity at a given time t, and q_e denotes the equilibrium adsorption capacity.[85]

Table 3. Kinetic model parameters for the adsorption of dyes onto **ZS-4** and **ZS-4@CNT**.

Model	**MB**				**MO**			
ZS-4								
Pseudo-first order	k_1 (min^{-1})	q_e (cal.) (mg g^{-1})	q_e (exp) (mg g^{-1})	R^2	k_1 (min^{-1})	q_e (cal.) (mg g^{-1})	q_e (exp) (mg g^{-1})	R^2
	0.0219	43.48	72.35	0.94013	0.0242	33.61	42.23	0.9808
Pseudo-second order	k_2 (g mg^{-1} min^{-1})	q_e (cal.) (mg g^{-1})	q_e (exp) (mg g^{-1})	R^2	k_2 (g mg^{-1} min^{-1})	q_e (cal.) (mg g^{-1})	q_e (exp) (mg g^{-1})	R^2
	0.00312	59.41	72.35	0.99005	0.00119	56.59	42.23	0.98526
Intraparticle diffusion	k_3 (mg g^{-1} min$^{-1/2}$)		R^2		k_3 (mg g^{-1} min$^{-1/2}$)		R^2	
	3.1671		0.81411		2.50189		0.94862	
ZS-4@CNT								
Pseudo-first order	k_1 (min^{-1})	q_e (cal.) (mg g^{-1})	q_e (exp) (mg g^{-1})	R^2	k_1 (min^{-1})	q_e (cal.) (mg g^{-1})	q_e (exp) (mg g^{-1})	R^2
	0.0252	62.99	114.45	0.88979	0.0242	39.93	43.15	0.99087
Pseudo-second order	k_2 (g mg^{-1} min^{-1})	q_e (cal.) (mg g^{-1})	q_e (exp) (mg g^{-1})	R^2	k_2 (g mg^{-1} min^{-1})	q_e (cal.) (mg g^{-1})	q_e (exp) (mg g^{-1})	R^2
	0.00258	106.53	114.45	0.99565	0.000711	50.45	43.15	0.98629
Intraparticle diffusion	k_3 (mg g^{-1} min$^{-1/2}$)		R^2		k_3 (mg g^{-1} min$^{-1/2}$)		R^2	
	3.590		0.80687		3.690		0.95024	

View Article Online
DOI: 10.1039/D5CE00684H

By applying this model, the corresponding kinetic parameters were derived. However, a notable discrepancy was observed between the experimentally obtained and the theoretically calculated q_e values, indicating a poor fit of the model to the experimental data. This mismatch, supported by the graphical results (**Fig. 12 and 13**), suggests that the pseudo-first order model is unsuitable for describing the adsorption behavior of the dyes on **ZS-4** and **ZS-4@CNT**. Further, pseudo-second order equation is given as:

$$\frac{t}{q_t} = \frac{1}{k_2 q_e^2} + \frac{t}{q_e} \qquad (4)$$

where k_2 (g mg^{-1} min^{-1}) is the rate constant specific to this model. This kinetic approach involves plotting t/q_t against time t. The resulting plots demonstrated excellent linearity, with correlation coefficients (R^2) very close to unity. Such a high degree of linearity strongly supports that the pseudo-second order model more accurately describes the adsorption mechanism of the cationic dyes onto **ZS-4** and **ZS-4@CNT**. This implies that the adsorption process is likely governed by chemisorption involving valence forces through sharing or exchange of electrons between adsorbent and adsorbate molecules.[86]

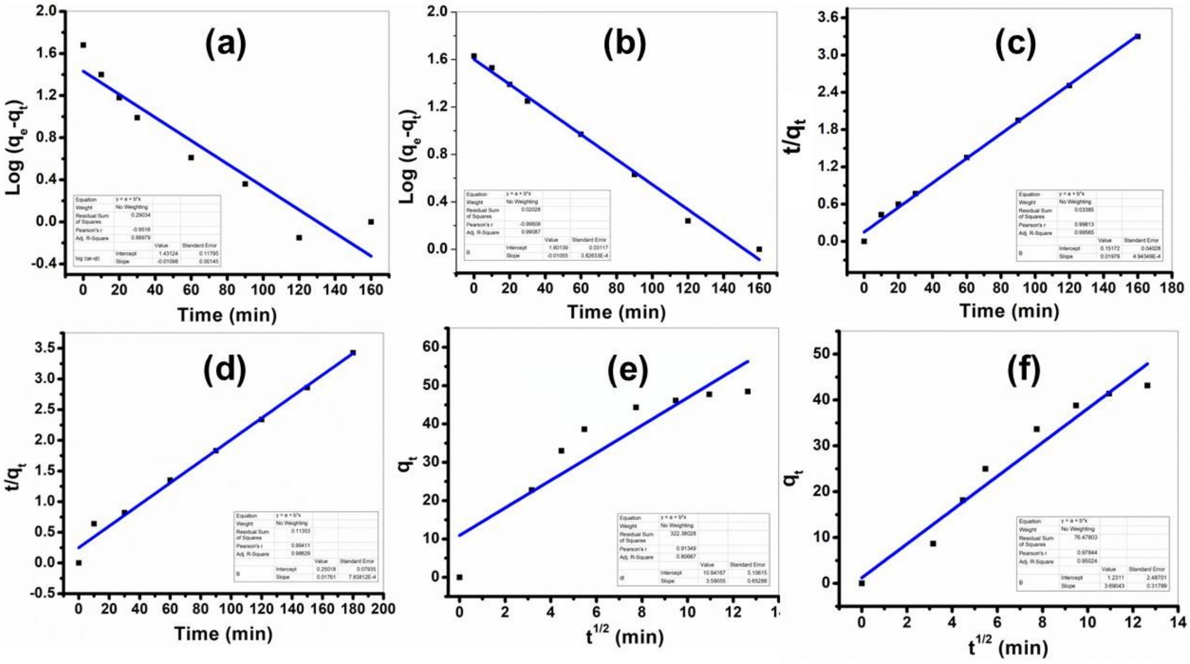

Fig. 12. Adsorption kinetics showing (a, b) pseudo-first order; (c, d) pseudo-second order; and (e, f) intraparticle diffusion models by **ZS-4**.

To further explore the diffusion mechanisms, the intraparticle diffusion model was also applied. Further, intraparticle diffusion equation is given as:

$$q_t = k_3\sqrt{t} \qquad (5)$$

View Article Online
DOI: 10.1039/D5CE00684H

Where k_3 (mg g^{-1} $min^{-1/2}$) represents rate constant, q_t as the adsorption capacity at a given time, and C as the intercept related to the boundary layer thickness. The kinetic parameters derived from this model, revealed inconsistencies between the calculated and experimental adsorption capacities. These deviations indicate that intraparticle diffusion is not the sole rate-controlling step in the overall adsorption process. In summary, among the models evaluated, the pseudo-second order kinetic model provides the best fit to the experimental data, suggesting that the adsorption of cationic dyes onto **ZS-4** and **ZS-4@CNT** predominantly follows a chemisorption mechanism. The pseudo-first order and intraparticle diffusion models, while offering some insights, were found inadequate for fully describing the adsorption kinetics observed in this study.[87]

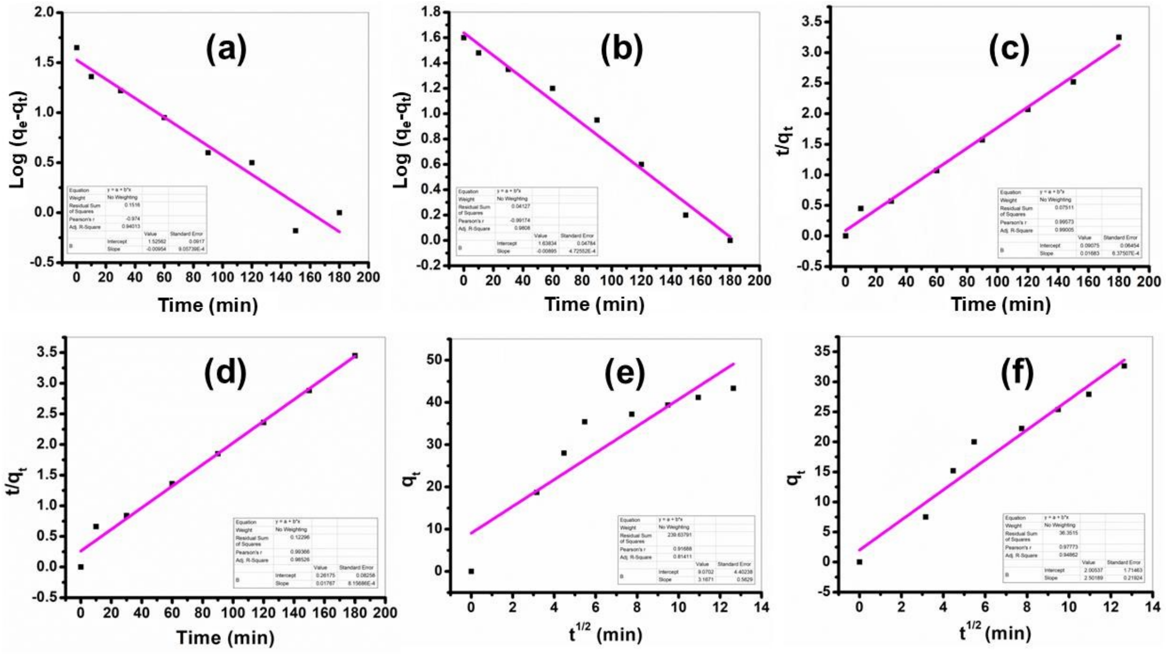

Fig. 13. Adsorption kinetics showing (a, b) pseudo-first order; (c, d) pseudo-second order; and (e, f) intraparticle diffusion models by **ZS-4@CNT**.

3.5.6 Adsorption mechanism

Adsorption is fundamentally a surface-driven phenomenon, profoundly influenced by the physical dimensions and morphology of the adsorbate, alongside the structural and functional characteristics of the adsorbent material. In the context of the present study, the dye molecules under investigation possess relatively large molecular sizes (**Table S8, Supporting Information**). Consequently, the encapsulation of dye molecules within the internal framework of **ZS-4@CNT** is not feasible. Instead, adsorption is restricted to interactions occurring at the external surfaces of **ZS-4@CNT** composite. Several interaction mechanisms have been widely reported in the literature to govern dye adsorption, including

View Article Online
DOI: 10.1039/D5CE00684H

hydrogen bonding, electrostatic interactions, ion-exchange processes, acid–base interactions, and π–π stacking interactions. In the present case, the adsorption of MB onto the **ZS-4@CNT** surfaces appears to be primarily facilitated through a synergistic contribution of electrostatic forces, hydrogen bonding, and π–π interactions. The cationic nature of MB molecules (MB^+) and the nucleophilic aromatic groups within the **ZS-4@CNT** framework foster strong electrostatic attractions, significantly enhancing the adsorption affinity for MB. This pronounced interaction likely accounts for the exceptionally high adsorption efficiency observed. Moreover, the linear structure of the MB molecule further favours its rapid diffusion and effective alignment with accessible adsorption sites on the polymer surface, accelerating the adsorption kinetics. In contrast, the adsorption behavior of MO^-, an anionic dye, was evidently different.[88-90]

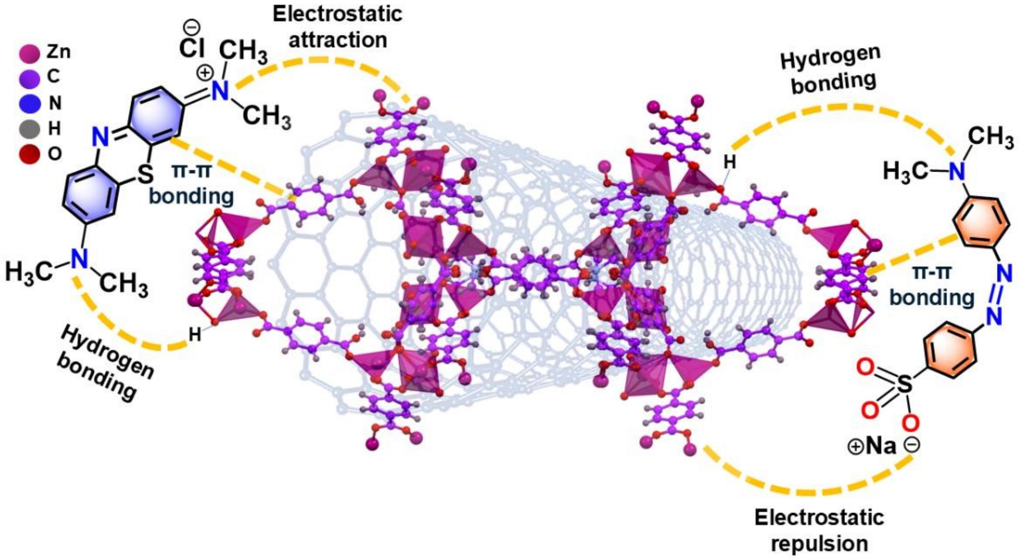

Fig. 14. Proposed mechanism for MB and MO dye adsorption using **ZS-4@CNT** composite.

The presence of negatively charged nucleophilic aromatic substituents on the **ZS-4** and **ZS-4@CNT** frameworks led to pronounced electrostatic repulsion with MO^- ions, culminating in the lowest adsorption capacity among the dyes studied. Nevertheless, it is worth noting that weak hydrogen bonding between the anionic functional groups of MO and hydrogen atoms of the **ZS-4** and **ZS-4@CNT'** aromatic ligands, along with π–π stacking interactions between the aromatic rings of the dye and the polymer, did facilitate a modest degree of MO adsorption, as illustrated in **Fig. 14**. Additionally, the structural attributes of the **ZS-4@CNT** notably influenced the adsorption efficiencies. The six-membered aromatic ring present in **ZS-4@CNT** enabled stronger π–π interactions with the aromatic systems of the dyes as a result, **ZS-4@CNT** exhibited superior adsorption capacity relative to **ZS-4**, reaffirming the critical role of framework topology in adsorption processes. Overall, these findings emphasize that, beyond specific interaction mechanisms, the molecular linearity of the dye plays a pivotal role in determining the adsorption rate and efficiency. Linear dye molecules are more readily adsorbed onto polymer surfaces, consistent with trends observed in previous studies.[91,92] Furthermore, a comparative overview of the adsorption performance of various reported metal organic materials for organic pollutant removal is provided in **Table S9 (Supporting Information).**

4. Conclusion

In summary, this study presents the successful synthesis of a novel zinc-based metal–organic framework, $\{(Me_2NH_2)_2[Zn_3(tpa)_4](DMF.3H_2O)\}_n$ **(ZS-4)**, designed using H_2TPA as the organic linker, featuring both tetrahedral and octahedral Zn(II) centers that support rare *bcg* and *bct* topologies. To enhance its adsorption performance, a composite (**ZS-4@CNT**) was fabricated by integrating CNTs into the **ZS-4** matrix, improving surface area and mechanical stability. Structural integrity and material properties were confirmed via FTIR, PXRD, SEM, TEM, TGA, BET, and XPS analyses. BET measurements revealed surface areas of 923.42 m^2/g for **ZS-4** and 1200.30 m^2/g for **ZS-4@CNT**. XPS data revealed peaks at 284.6 eV (C–C/C=C), 286.0 eV (C–O/C–OH), and 288.5 eV (O–C=O) in the C 1s spectrum. The O 1s region showed peaks at 531.8 eV (C=O) and 533.0 eV (C–OH). Zn 2p peaks at 1022.8 eV and 1042.7 eV confirmed the presence of Zn^{2+} ions. The composite showed superior dye adsorption, removing 66% MB and 36.3% MO within 20 minutes. Maximum adsorption capacities were 114.45 mg/g for MB and 43.15 mg/g for MO with the composite. Kinetic modeling confirmed pseudo-second-order behavior, indicating chemisorption. This study demonstrates how combining dual-zinc coordination with CNT integration yields high-performance adsorbents for sustainable water purification applications.

Acknowledgement

Mohd Zeeshan thanks MHRD, Govt of India for providing Prime Minister's Research Fellowship (PMRF). Authors are thankful to the Ongoing Research Funding program (ORF2025-379), King Saud University, Riyadh, Saudi Arabia for supporting this work.

References

(1) Hu, W.; Yang, Q.; Wang, R.; Chen, Q.; Kong, Y. Efficient Adsorptive Removal of Two Anionic Dyes (Methyl Orange and Methyl Red) with MOF-525: Adsorption Isotherms and Kinetics Studies. *Environ. Prog. Sustain. Energy* **2025**, *44* (2), e14543.

(2) Hazarika, U. N.; Pegu, A.; Devi, S.; Konwer, S.; Singh, M. K.; Gogoi, S.; Pegu, M.; Khakhlary, P. An Anionic Metal–Organic Framework and Its r-Graphene Oxide Composite for Selective Adsorption and Separation of Methyl Blue from Aqueous Solution. *Dalt. Trans.* **2025**, *54* (10), 4112–4119.

(3) Huang, G.; Zhang, Y.; Zhang, R.; Zhang, M.; Zhang, L.; Xin, Y.; Liu, Y.; Chen, J. Removal of Methyl Orange and Methylene Blue by Bimetallic Zinc/Cobalt Metal–Organic Skeleton/Carbon Nanotubes (Zn/Co-ZIF@ CNTs). *RSC Adv.* **2025**, *15* (6), 4681–4692.

(4) Li, Y.; Li, D.; Zheng, Y.; Lu, S.; Cai, Y.; Dong, R. Biohybrid Microrobots with a Spirulina Skeleton and MOF Skin for Efficient Organic Pollutant Adsorption. *Nanoscale* **2025**, *17* (12), 7035–7044.

(5) Shadigoo, R.; Salimi, F.; Azimi, N. Experimental Study on a Modified Metal–Organic Framework Catalyst for the Removal of Methylene Blue. *Res. Chem. Intermed.* **2025**, 51(6), 1–22.

(6) Koppula, S.; Manabolu Surya, S.; Katari, N. K.; Dhami, P. S.; Sivasankaran Nair, R. K. Mesoporous MOF Composite for Efficient Removal of Uranium, Methyl Orange, Methylene Blue, and Congo Red Dyes from Aqueous Solutions. *Appl. Organomet. Chem.* **2022**, *36* (3), e6554.

(7) Lv, S.-W.; Liu, J.-M.; Ma, H.; Wang, Z.-H.; Li, C.-Y.; Zhao, N.; Wang, S. Simultaneous Adsorption of Methyl Orange and Methylene Blue from Aqueous Solution Using Amino Functionalized Zr-Based MOFs. *Microporous Mesoporous Mater.* **2019**, *282*, 179–187.

(8) Naeem, A.; Saeed, T.; Sayed, M.; Ahmad, B.; Mahmood, T.; Farooq, M.; Perveen, F. Chitosan Decorated Zirconium Metal-Organic Framework for Collaborative Adsorption and Photocatalytic Degradation of Methylene Blue and Methyl Orange. *Process Saf. Environ. Prot.* **2023**, *176*, 115–130.

(9) Dinh, H. T.; Tran, N. T.; Trinh, D. X. Investigation into the Adsorption of Methylene Blue and Methyl Orange by UiO-66-NO2 Nanoparticles. *J. Anal. Methods Chem.* **2021**, *2021* (1), 5512174.

(10) Ramírez, D. J.; Herrera, L. A. A.; Colorado-Peralta, R.; Rodríguez, R. P.; Reyes, P. K. C.; Chiñas, L. E.; Sánchez, M.; Rivera, J. M. Highly Efficient Methyl Orange Adsorption by UV-012, a New Crystalline Co (Ii) MOF. *CrystEngComm* **2021**, *23* (19), 3537–3548.

(11) Adawiah, A.; Yudhi, M. D. L.; Zulys, A. Photocatalytic Degradation of Methylene Blue and Methyl Orange by Y-PTC Metal-Organic Framework. *J. Kim. Val.* **2021**, *7* (2), 129–141.

(12) Podborska, A.; Luty-Błocho, M. Molecular Structure of Methyl Orange and Its Role in the Process of [Pd (Azo)] Compound and MOF Formation. *J. Mol. Struct.* **2023**, *1273*, 134312.

(13) Karami, A.; Sabouni, R.; Al-Sayah, M. H.; Aidan, A. Adsorption Potentials of Iron-Based Metal–Organic Framework for Methyl Orange Removal: Batch and Fixed-Bed Column Studies. *Int. J. Environ. Sci. Technol.* **2021**, 1–16.

(14) Muslim, M.; Ali, A.; Neogi, I.; Dege, N.; Shahid, M.; Ahmad, M. Facile Synthesis, Topological Study, and Adsorption Properties of a Novel Co (II)-Based Coordination Polymer for Adsorptive Removal of Methylene Blue and Methyl Orange Dyes. *Polyhedron* **2021**, *210*, 115519.

View Article Online
DOI: 10.1039/D5CE00684H

(15) Zeeshan, M.; Shahid, M. State of the Art Developments and Prospects of Metal–Organic Frameworks for Energy Applications. *Dalt. Trans.* **2022**, *51* (5), 1675–1723.

(16) Shamim, M. A.; Zia, H.; Zeeshan, M.; Khan, M. Y.; Shahid, M. Metal Organic Frameworks (MOFs) as a Cutting-Edge Tool for the Selective Detection and Rapid Removal of Heavy Metal Ions from Water: Recent Progress. *J. Environ. Chem. Eng.* **2022**, *10* (1), 106991.

(17) Zia, H.; Shamim, M. A.; Zeeshan, M.; Khan, M. Y.; Shahid, M. Metal Organic Frameworks as a Versatile Platform for the Radioactive Iodine Capture: State of the Art Developments and Future Prospects. *Inorganica Chim. Acta* **2022**, *539*, 121026.

(18) Khan, M. Y.; Husain, A.; Mahajan, D. K.; Muaz, M.; Shahid, M.; Zeeshan, M.; Sama, F.; Ahmad, S. Facile Synthesis of a Three-Dimensional Ln-MOF@ FCNT Composite for the Fabrication of a Symmetric Supercapacitor Device with Ultra-High Energy Density: Overcoming the Energy Storage Barrier. *Dalt. Trans.* **2024**, *53* (17), 7477–7497.

(19) Akmal, S. A.; Khalid, M.; Ahmad, M. S.; Shahid, M.; Ahmad, M. Interwoven Architectural Complexity in Ni (II) Ion-Based 3D MOF Using Bipyridine and Tetrabenzenecarboxylic Acid: Adsorption Insights in Highly Efficient Iodine and Cationic Dye Capture. *Cryst. Growth Des.* **2024**, *24* (17), 7173–7193.

(20) Qasem, K. M. A.; Khan, M. Y.; Akmal, S. A.; Saleh, H. A. M.; Mehtab, M.; Shahid, M.; Salem, M. A. S.; Khan, M. M. A.; Ghanem, Y. S. A.; Malik, A. Highly Efficient Iodine Capture and Selective Adsorption and Removal of Cationic Dyes by Using a Copper-Based Coordination Polymer Decorated over Graphene Oxide and Carbon Nanotubes. *J. Water Process Eng.* **2025**, *69*, 106569.

(21) Siddique, A.; Mantasha, I.; Rawat, P.; Singh, R. N.; Shahid, M.; Trivedi, S.; Gautam, A.; Zeeshan, M. A New Zn (Ii) MOF Assembled from Metal–Organic Cubes (MOCs) as a Highly Efficient Adsorbent for Cationic Dyes. *CrystEngComm* **2021**, *23* (11), 2316–2325.

(22) Mantasha, I.; Hussain, S.; Ahmad, M.; Shahid, M. Two Dimensional (2D) Molecular Frameworks for Rapid and Selective Adsorption of Hazardous Aromatic Dyes from Aqueous Phase. *Sep. Purif. Technol.* **2020**, *238*, 116413.

(23) Iman, K.; Shahid, M.; Khan, M. S.; Ahmad, M.; Sama, F. Topology, Magnetism and Dye Adsorption Properties of Metal Organic Frameworks (MOFs) Synthesized from Bench Chemicals. *CrystEngComm* **2019**, *21* (35), 5299–5309.

(24) Mariyam, A.; Shahid, M.; I, M.; Khan, M. S.; Ahmad, M. S. Tetrazole Based Porous Metal Organic Framework (MOF): Topological Analysis and Dye Adsorption Properties. *J. Inorg. Organomet. Polym. Mater.* **2020**, *30*, 1935–1943.

(25) Asad, M.; Anwar, M. I.; Abbas, A.; Younas, A.; Hussain, S.; Gao, R.; Li, L.-K.; Shahid, M.; Khan, S. AIE Based Luminescent Porous Materials as Cutting-Edge Tool for Environmental Monitoring: State of the Art Advances and Perspectives. *Coord. Chem. Rev.* **2022**, *463*, 214539.

View Article Online
DOI: 10.1039/D5CE00684H

(26) Kamal, S.; Khalid, M.; Khan, M. S.; Shahid, M. Metal Organic Frameworks and Their Composites as Effective Tools for Sensing Environmental Hazards: An up-to-Date Tale of Mechanism, Current Trends and Future Prospects. *Coord. Chem. Rev.* **2023**, *474*, 214859.

(27) Kamal, S.; Khalid, M.; Khan, M. S.; Shahid, M.; Ahmad, M. Breathing Transition and Effective Iodine Adsorption in a Temperature-Responsive Zn-Based Flexible Metal–Organic Framework. *Langmuir* **2024**, *41* (1), 1182–1193.

(28) Khan, S.; Lone, A. R.; Khan, M. Y.; Rahaman, S.; Pandey, K.; Helal, A.; Sama, F.; Shahid, M. Engineered Amine-Functionalized Metal–Organic Framework to Fabricate a Composite for Next-Generation Asymmetric Supercapacitors with Ultrahigh Performance: Modulating the Energy Storage Barrier. *Langmuir* **2024**, *40* (40), 21106–21119.

(29) Anwar, M. I.; Asad, M.; Ma, L.; Zhang, W.; Abbas, A.; Khan, M. Y.; Zeeshan, M.; Khatoon, A.; Gao, R.; Manzoor, S. Nitrogenous MOFs and Their Composites as High-Performance Electrode Material for Supercapacitors: Recent Advances and Perspectives. *Coord. Chem. Rev.* **2023**, *478*, 214967.

(30) Khan, M. Y.; Shahid, M. A Contemporary Report on Explications of Flexible Metal-Organic Frameworks with Regards to Structural Simulation, Dynamics and Material Applications. *Polyhedron* **2022**, 116041.

(31) Zeeshan, M.; Kumar, M.; Ansari, A.; Alarifi, A.; Li, X.; Ghanem, Y. S. A.; Khan, M. Y.; Islam, M. A. S.; Touqeer, Q.; Rashid, H. Pyridine-2, 4-Dicarboxylate as an Organic Chelating Ligand towards Cobalt (II) for Designing a Novel Complex: X-Ray Studies, DFT Analysis, and Evaluation of Catechol Oxidase Mimic Activity and Anticancer Property towards A549 Cell Line. *Inorganica Chim. Acta* **2025**, 122663.

(32) Saleh, H. A. M.; Khan, S.; Kumar, M.; Ansari, A.; Shahid, M.; Sama, F.; Qasem, K. M. A.; Khan, M. Y.; Mehtab, M.; Ahmad, M. Fabrication of Unique Mixed-Valent CoICoII and CuICuII Metal–Organic Frameworks (MOFs) for Desulfurization of Fuels: A Combined Experimental and Theoretical Approach toward Green Fuel. *Inorg. Chem.* **2023**, *63* (1), 329–345.

(33) Zeeshan, M.; Khan, M. Y.; Khan, R.; Mehtab, M.; Shahid, M. Turning CO_2 into Treasure: The Promise of Metal–Organic Frameworks. *CrystEngComm* **2024**, *26* (39), 5489–5517.

(34) Zeeshan, M.; Khan, M. Y.; Shahid, M.; Ikram, S.; Ahmad, M. Engineering Cost-Effective N-Rich Metal-Organic Frameworks (MOFs) for Highly Efficient CO2 Capture and Its Catalytic Conversion to Cyclic Carbonates: A Step towards Sustainable Carbon Utilization. *Dalt. Trans.* **2025**, 54, 11398.

(35) Jannah, M.; Hidayat, A. R. P.; Martak, F.; Ediati, R. Solvothermal Synthesis of Zr-Based MOFs with Mixed Linker as Adsorbent for Methyl Orange in Water. In *IOP Conference Series: Earth and Environmental Science*; IOP Publishing, **2024**; Vol. 1388, p 12013.

(36) Tran, K. N. T.; Phan, C. P. K.; Ho, V. T.; Chau, H. D.; Nguyen, T. N. D. Adsorption of

Methyl Orange Dyes on Oriented Co/Fe-MOF Bimetallic Organic Framework in Wastewater Treatment. *Indones. J. Chem.* **2023**, *23* (2), 533–541.

(37) Wu, L.; Liu, X.; Lv, G.; Zhu, R.; Tian, L.; Liu, M.; Li, Y.; Rao, W.; Liu, T.; Liao, L. Study on the Adsorption Properties of Methyl Orange by Natural One-Dimensional Nano-Mineral Materials with Different Structures. *Sci. Rep.* **2021**, *11* (1), 10640.

(38) Zhang, W.; Huang, T.; Ren, Y.; Wang, Y.; Yu, R.; Wang, J.; Tu, Q. Preparation of Chitosan Crosslinked with Metal-Organic Framework (MOF-199)@ Aminated Graphene Oxide Aerogel for the Adsorption of Formaldehyde Gas and Methyl Orange. *Int. J. Biol. Macromol.* **2021**, *193*, 2243–2251.

(39) Luong, T. H. V; Nguyen, T. H. T.; Nguyen, B. V; Nguyen, N. K.; Nguyen, T. Q. C.; Dang, G. H. Efficient Degradation of Methyl Orange and Methylene Blue in Aqueous Solution Using a Novel Fenton-like Catalyst of CuCo-ZIFs. *Green Process. Synth.* **2022**, *11* (1), 71–83.

(40) Abbou, B.; Lebkiri, I.; Ouaddari, H.; El Amri, A.; Achibat, F. E.; Kadiri, L.; Ouass, A.; Lebkiri, A.; Rifi, E. H. Improved Removal of Methyl Orange Dye by Adsorption Using Modified Clay: Combined Experimental Study Using Surface Response Methodology. *Inorg. Chem. Commun.* **2023**, *155*, 111127.

(41) Zhang, X.; Qian, L.; Yang, S.; Peng, Y.; Xiong, B.; Li, J.; Fang, P.; He, C. Comparative Studies of Methyl Orange Adsorption in Various Metal-Organic Frameworks by Nitrogen Adsorption and Positron Annihilation Lifetime Spectroscopy. *Microporous Mesoporous Mater.* **2020**, *296*, 109993.

(42) Ahsan, M. A.; Fernandez-Delgado, O.; Deemer, E.; Wang, H.; El-Gendy, A. A.; Curry, M. L.; Noveron, J. C. Carbonization of Co-BDC MOF Results in Magnetic C@ Co Nanoparticles That Catalyze the Reduction of Methyl Orange and 4-Nitrophenol in Water. *J. Mol. Liq.* **2019**, *290*, 111059.

(43) Ahmad, N.; Younus, H. A.; Chughtai, A. H.; Van Hecke, K.; Khattak, Z. A. K.; Gaoke, Z.; Danish, M.; Verpoort, F. Synthesis of 2D MOF Having Potential for Efficient Dye Adsorption and Catalytic Applications. *Catal. Sci. Technol.* **2018**, *8* (16), 4010–4017.

(44) Dang, A.; Doan, T.; Huyen, P. T. Embed CdS into MIL-101 to Boost the Photocatalytic Activity for Methylene Blue and Methyl Orange Degradation in the Visible Range. *Water, Air, Soil Pollut.* **2024**, *235* (2), 156.

(45) Murtaza, S. Z. M.; Shomal, R.; Sabouni, R.; Ghommem, M. Facile Metal Organic Framework Composites as Photocatalysts for Lone/Simultaneous Photodegradation of Naproxen, Ibuprofen and Methyl Orange. *Environ. Technol. Innov.* **2022**, *27*, 102751.

(46) Ahsan, M. A.; Deemer, E.; Fernandez-Delgado, O.; Wang, H.; Curry, M. L.; El-Gendy, A. A.; Noveron, J. C. Fe Nanoparticles Encapsulated in MOF-Derived Carbon for the Reduction of 4-Nitrophenol and Methyl Orange in Water. *Catal. Commun.* **2019**, *130*, 105753.

(47) Khan, M. I.; Shanableh, A.; Elboughdiri, N.; Lashari, M. H.; Manzoor, S.; Shahida, S.; Farooq, N.; Bouazzi, Y.; Rejeb, S.; Elleuch, Z. Adsorption of Methyl Orange from an Aqueous Solution onto a BPPO-Based Anion Exchange Membrane. *ACS omega* **2022**, *7* (30), 26788–26799.

(48) Ibers, J. A.; Hamilton, W. C. *International Tables for X-Ray Crystallography*; Reidel. 1983.

(49) SMART & SAINT, Software Reference Manuals, Version 6.45, *Bruker Analytical X-ray Systems, Inc., Madison*, 2003.

(50) Sheldrick, G. M.; Sheldrick, SADABS, software for empirical absorption correction, Ver. 2.05, *University of Göttingen, Göttingen, Germany*, 2002.

(51) XPREP, version 5.1, *Siemens Industrial Automation Inc., Madison, WI*, 1995.

(52) Dolomanov, O. V.; Bourhis, L. J.; Gildea, R. J.; Howard, J. A. K.; Puschmann, H. Olex2: A Complete Structure Solution, Refinement and Analysis Program. *J. Appl. Cryst.* **2009**, *42*, 339-341.

(53) Islam, M. T.; Saenz-Arana, R.; Hernandez, C.; Guinto, T.; Ahsan, M. A.; Bragg, D. T.; Wang, H.; Alvarado-Tenorio, B.; Noveron, J. C. Conversion of Waste Tire Rubber into a High-Capacity Adsorbent for the Removal of Methylene Blue, Methyl Orange, and Tetracycline from Water. *J. Environ. Chem. Eng.* **2018**, *6* (2), 3070–3082.

(54) Kavak, S.; Kulak, H.; Polat, H. M.; Keskin, S.; Uzun, A. Fast and Selective Adsorption of Methylene Blue from Water Using [BMIM][PF6]-Incorporated UiO-66 and NH2-UiO-66. *Cryst. Growth Des.* **2020**, *20* (6), 3590–3595.

(55) del Rio, M.; Escarabajal, J. C. G.; Palomino, G. T.; Cabello, C. P. Zinc/Iron Mixed-Metal MOF-74 Derived Magnetic Carbon Nanorods for the Enhanced Removal of Organic Pollutants from Water. *Chem. Eng. J.* **2022**, *428*, 131147.

(56) Asadi, E.; Bakherad, M.; Ghasemi, M. H. High and Selective Adsorption of Methylene Blue Using N-Rich, Microporous Metal–Organic Framework [ZnBT (H2O) 2] N. *J. Iran. Chem. Soc.* **2022**, *19* (1), 173–185.

(57) Boubkr, L.; Bhakta, A. K.; Snoussi, Y.; Moreira Da Silva, C.; Michely, L.; Jouini, M.; Ammar, S.; Chehimi, M. M. Highly Active Ag-Cu Nanocrystal Catalyst-Coated Brewer’s Spent Grain Biochar for the Mineralization of Methyl Orange and Methylene Blue Dye Mixture. *Catalysts* **2022**, *12* (11), 1475.

(58) Nazir, M. A.; Khan, N. A.; Cheng, C.; Shah, S. S. A.; Najam, T.; Arshad, M.; Sharif, A.; Akhtar, S.; ur Rehman, A. Surface Induced Growth of ZIF-67 at Co-Layered Double Hydroxide: Removal of Methylene Blue and Methyl Orange from Water. *Appl. Clay Sci.* **2020**, *190*, 105564.

(59) Islam, M. A.; Ahmed, M. J.; Khanday, W. A.; Asif, M.; Hameed, B. H. Mesoporous Activated Carbon Prepared from NaOH Activation of Rattan (Lacosperma Secundiflorum) Hydrochar for Methylene Blue Removal. *Ecotoxicol. Environ. Saf.* **2017**, *138*, 279–285.

(60) Kayan, G. Ö.; Kayan, A. Inorganic–Organic Hybrid Materials of Zirconium and Aluminum and Their Usage in the Removal of Methylene Blue. *J. Inorg. Organomet. Polym. Mater.* **2021**, *31* (8), 3613–3623

(61) Parale, V. G.; Choi, H.; Kim, J.; Lee, W.; Kim, S.-H.; Jung, W. K.; Park, H.-H.

Investigation of Compound State of SiO2-TiO2 Aerogel Synthesized through Controlled Sol-Gel Reaction. *J. Alloys Compd.* **2024**, *980*, 173561.

(62) Refat, M. S.; Saad, H. A.; Gobouri, A. A.; Alsawat, M.; Adam, A. M. A.; Shakya, S.; Gaber, A.; Alsuhaibani, A. M.; El-Megharbel, S. M. Synthesis and Spectroscopic Characterizations of Nanostructured Charge Transfer Complexes Associated between Moxifloxacin Drug Donor and Metal Chloride Acceptors as a Catalytic Agent in a Recycling of Wastewater. *J. Mol. Liq.* **2022**, *349*, 118121.

(63) Paiman, S. H.; Rahman, M. A.; Uchikoshi, T.; Abdullah, N.; Othman, M. H. D.; Jaafar, J.; Abas, K. H.; Ismail, A. F. Functionalization Effect of Fe-Type MOF for Methylene Blue Adsorption. *J. Saudi Chem. Soc.* **2020**, *24* (11), 896–905.

(64) Darwish, A. A. A.; Rashad, M.; AL-Aoh, H. A. Methyl Orange Adsorption Comparison on Nanoparticles: Isotherm, Kinetics, and Thermodynamic Studies. *Dye. Pigment.* **2019**, *160*, 563–571.

(65) Gao, L.; Gao, T.; Zhang, Y.; Hu, T. A Bifunctional 3D Porous Zn-MOF: Fluorescence Recognition of Fe3+ and Adsorption of Congo Red/Methyl Orange Dyes in Aqueous Medium. *Dye. Pigment.* **2022**, *197*, 109945.

(66) Arora, C.; Soni, S.; Sahu, S.; Mittal, J.; Kumar, P.; Bajpai, P. K. Iron Based Metal Organic Framework for Efficient Removal of Methylene Blue Dye from Industrial Waste. *J. Mol. Liq.* **2019**, *284*, 343–352.

(67) El Naga, A. O. A.; Shaban, S. A.; El Kady, F. Y. A. Metal Organic Framework-Derived Nitrogen-Doped Nanoporous Carbon as an Efficient Adsorbent for Methyl Orange Removal from Aqueous Solution. *J. Taiwan Inst. Chem. Eng.* **2018**, *93*, 363–373.

(68) Li, X.; Yuan, H.; Quan, X.; Chen, S.; You, S. Effective Adsorption of Sulfamethoxazole, Bisphenol A and Methyl Orange on Nanoporous Carbon Derived from Metal-Organic Frameworks. *J. Environ. Sci.* **2018**, *63*, 250–259.

(69) Wang, C.; Feng, X.; Shang, S.; Liu, H.; Song, Z.; Zhang, H. Adsorption of Methyl Orange from Aqueous Solution with Lignin-Modified Metal–Organic Frameworks: Selective Adsorption and High Adsorption Capacity. *Bioresour. Technol.* **2023**, *388*, 129781.

(70) Yang, Q.; Ren, S.; Zhao, Q.; Lu, R.; Hang, C.; Chen, Z.; Zheng, H. Selective Separation of Methyl Orange from Water Using Magnetic ZIF-67 Composites. *Chem. Eng. J.* **2018**, *333*, 49–57.

(71) Farasati Far, B.; Naimi-Jamal, M. R.; Jahanbakhshi, M.; Keihankhadiv, S.; Baradarbarjastehbaf, F. Enhanced Methylene Blue Adsorption Using Single-Walled Carbon Nanotubes/Chitosan-Graft-Gelatin Nanocomposite Hydrogels. *Sci. Rep.* **2024**, *14* (1), 19217.

(72) Song, G.; Li, A.; Shi, Y.; Li, W.; Wang, H.; Wang, C.; Li, R.; Ding, G. Sorptive Removal of Methylene Blue from Water by Magnetic Multi-Walled Carbon Nanotube Composites. *Environ. Sci. Pollut. Res.* **2021**, *28*, 41268–41282.

(73) Baig, M. T.; Kayan, A. Advanced Biopolymer-Based Ti/Si-Terephthalate Hybrid Materials for Sustainable and Efficient Adsorption of the Tetracycline Antibiotic. *Int. J.*

View Article Online
DOI: 10.1039/D5CE00684H

Biol. Macromol. **2024**, *280*, 135676.

(74) Hossain, M. A.; Mondol, M. M. H.; Jhung, S. H. Functionalized Metal-Organic Framework-Derived Carbon: Effective Adsorbent to Eliminate Methylene Blue, a Small Cationic Dye from Water. *Chemosphere* **2022**, *303*, 134890.

(75) Liu, Z.; He, W.; Zhang, Q.; Shapour, H.; Bakhtari, M. F. Preparation of a GO/MIL-101 (Fe) Composite for the Removal of Methyl Orange from Aqueous Solution. *ACS omega* **2021**, *6* (7), 4597–4608.

(76) Demirci, G. V.; Baig, M. T.; Kayan, A. UiO-66 MOF/Zr-Di-Terephthalate/Cellulose Hybrid Composite Synthesized via Sol-Gel Approach for the Efficient Removal of Methylene Blue Dye. *Int. J. Biol. Macromol.* **2024**, *283*, 137950.

(77) Baig, M. T.; Kayan, A. Eco-Friendly Novel Adsorbents Composed of Hybrid Compounds for Efficient Adsorption of Methylene Blue and Congo Red Dyes: Kinetic and Thermodynamic Studies. *Sep. Sci. Technol.* **2023**, *58* (5), 862–883.

(78) Herrera, L. Á. A.; Reyes, P. K. C.; Flores, A. M. H.; Martínez, L. T.; Villanueva, J. M. R. BDC-Zn MOF Sensitization by MO/MB Adsorption for Photocatalytic Hydrogen Evolution under Solar Light. *Mater. Sci. Semicond. Process.* **2020**, *109*, 104950.

(79) Mantasha, I.; Shahid, M.; Saleh, H. A. M.; Qasem, K. M. A.; Ahmad, M. A Novel Sustainable Metal Organic Framework as the Ultimate Aqueous Phase Sensor for Natural Hazards: Detection of Nitrobenzene and F− at the Ppb Level and Rapid and Selective Adsorption of Methylene Blue. *CrystEngComm* **2020**, *22* (22), 3891–3909.

(80) Zhang, Y.; Li, Y.; Wang, M.; Chen, B.; Sun, Y.; Chen, K.; Du, Q.; Pi, X.; Wang, Y. Adsorption of Methylene Blue from Aqueous Solution Using Gelatin-Based Carboxylic Acid-Functionalized Carbon Nanotubes@ Metal–Organic Framework Composite Beads. *Nanomaterials* **2022**, *12* (15), 2533.

(81) Jedynak, K.; Repelewicz, M.; Kurdziel, K.; Wideł, D. Mesoporous Carbons as Adsorbents to Removal of Methyl Orange (Anionic Dye) and Methylene Blue (Cationic Dye) from Aqueous Solutions. *Desalin. Water Treat.* **2021**, *220*, 363–379.

(82) El Naga, A. O. A.; Shaban, S. A.; El Kady, F. Y. A. Metal Organic Framework-Derived Nitrogen-Doped Nanoporous Carbon as an Efficient Adsorbent for Methyl Orange Removal from Aqueous Solution. *J. Taiwan Inst. Chem. Eng.* **2018**, *93*, 363–373.

(83) Ramírez, D. J.; Herrera, L. A. A.; Colorado-Peralta, R.; Rodríguez, R. P.; Reyes, P. K. C.; Chiñas, L. E.; Sánchez, M.; Rivera, J. M. Highly Efficient Methyl Orange Adsorption by UV-012, a New Crystalline Co (Ii) MOF. *CrystEngComm* **2021**, *23* (19), 3537–3548.

(84) Jin, L.; Zhao, X.; Qian, X.; Dong, M. Nickel Nanoparticles Encapsulated in Porous Carbon and Carbon Nanotube Hybrids from Bimetallic Metal-Organic-Frameworks for Highly Efficient Adsorption of Dyes. *J. Colloid Interface Sci.* **2018**, *509*, 245–253.

(85) Abualnaja, K. M.; Alprol, A. E.; Abu-Saied, M. A.; Mansour, A. T.; Ashour, M. Studying the Adsorptive Behavior of Poly (Acrylonitrile-Co-Styrene) and Carbon Nanotubes (Nanocomposites) Impregnated with Adsorbent Materials towards Methyl Orange Dye. *Nanomaterials* **2021**, *11* (5), 1144.

(86) Cheng, P.; Wang, X.; Markus, J.; Wahab, M. A.; Chowdhury, S.; Xin, R.; Alshehri, S.

View Article Online
DOI: 10.1039/D5CE00684H

M.; Bando, Y.; Yamauchi, Y.; Kaneti, Y. V. Carbon Nanotube-Decorated Hierarchical Porous Nickel/Carbon Hybrid Derived from Nickel-Based Metal-Organic Framework for Enhanced Methyl Blue Adsorption. *J. Colloid Interface Sci.* **2023**, *638*, 220–230.

(87) Lv, S.-W.; Liu, J.-M.; Ma, H.; Wang, Z.-H.; Li, C.-Y.; Zhao, N.; Wang, S. Simultaneous Adsorption of Methyl Orange and Methylene Blue from Aqueous Solution Using Amino Functionalized Zr-Based MOFs. *Microporous Mesoporous Mater.* **2019**, *282*, 179–187.

(88) Wu, L.; Liu, X.; Lv, G.; Zhu, R.; Tian, L.; Liu, M.; Li, Y.; Rao, W.; Liu, T.; Liao, L. Study on the Adsorption Properties of Methyl Orange by Natural One-Dimensional Nano-Mineral Materials with Different Structures. *Sci. Rep.* **2021**, *11* (1), 10640.

(89) Athari, M.; Fattahi, M.; Khosravi-Nikou, M.; Hajhariri, A. Adsorption of Different Anionic and Cationic Dyes by Hybrid Nanocomposites of Carbon Nanotube and Graphene Materials over UiO-66. *Sci. Rep.* **2022**, *12* (1), 20415.

(90) Li, X.; Yuan, H.; Quan, X.; Chen, S.; You, S. Effective Adsorption of Sulfamethoxazole, Bisphenol A and Methyl Orange on Nanoporous Carbon Derived from Metal-Organic Frameworks. *J. Environ. Sci.* **2018**, *63*, 250–259.

(91) Oveisi, M.; Asli, M. A.; Mahmoodi, N. M. Carbon Nanotube Based Metal-Organic Framework Nanocomposites: Synthesis and Their Photocatalytic Activity for Decolorization of Colored Wastewater. *Inorganica Chim. Acta* **2019**, *487*, 169–176.

(92) Huang, G.; Zhang, Y.; Zhang, R.; Zhang, M.; Zhang, L.; Xin, Y.; Liu, Y.; Chen, J. Removal of Methyl Orange and Methylene Blue by Bimetallic Zinc/Cobalt Metal–Organic Skeleton/Carbon Nanotubes (Zn/Co-ZIF@ CNTs). *RSC Adv.* **2025**, *15* (6), 4681–4692.

Data will be made available on request.

View Article Online
DOI: 10.1039/D5CE00684H